minerals

Article

Aqueous Carbonation of Waste Incineration Residues: Comparing BA, FA, and APCr Across Production Scenarios

Quentin Wehrung [1,*], Davide Bernasconi [1], Enrico Destefanis [1], Caterina Caviglia [1], Nadia Curetti [1], Sara Di Felice [1], Erica Bicchi [2,3], Alessandro Pavese [1] and Linda Pastero [1,4]

[1] Earth Sciences Department, University of Turin, Via Valperga Caluso, 35, 10125 Torino, Italy; davide.bernasconi@unito.it (D.B.); enrico.destefanis@unito.it (E.D.); caterina.caviglia@unito.it (C.C.); nadia.curetti@unito.it (N.C.); sara.difelice@edu.unito.it (S.D.F.); alessandro.pavese@unito.it (A.P.); linda.pastero@unito.it (L.P.)

[2] LPG (Planetology and Geosciences Laboratory), University of Angers, 2 Boulevard Lavoisier, CEDEX 01, 49045 Angers, France; ebicchi@esaip.org

[3] ESAIP La Salle Graduate School of Engineering, 18 Rue du 8 mai 1945, 49124 Saint-Barthélemy d'Anjou, France

[4] NIS-Nanomaterials for Industry and Sustainability Inter-Departmental Centre, Università degli Studi di Torino, Via Quarello 16, 10135 Torino, Italy

* Correspondence: quentin.wehrung@unito.it; Tel.: +39-33663281762

Abstract: This study investigates the reactivity of municipal solid waste incineration residues to aqueous carbonation, focusing on CO_2 absorption rates, uptakes, and heavy metal (HM) leachability. Various combinations of boiler, electrofilter, and bag filter residues were assessed under typical incineration conditions. Bag filter residues from lime-sorbent plants exhibited the highest CO_2 uptake (244.5 gCO_2/kg), while bottom ash (BA) fine fraction, boiler/electrofilter fly ash (FA), and other mixed air pollution control residue (APCr) demonstrated uptakes of 101, 0, 93, and 167 gCO_2/kg, respectively. Carbonation kinetics revealed that high calcium content FA and APCr, followed similar CO_2 absorption trends. Notably, BA carbonation was predominantly driven by Ca-aluminates rather than lime. Carbonation reduces leaching of Al, As, Cd, Co, Cu, Ni, Pb and Zn compared to water washing, though significant concerns arise with anions such as Sb and Cr. In BA, critical behaviours of Cr, Mn, and Fe were observed, with Cr leaching likely controlled by Fe-Mn-Cr oxide particle dissolution. These findings highlight the potential of integrating enhanced metal recovery (EMR) through density or magnetic separation in BA prior to carbonation to reduce HM leaching and recycle critical metals (Ag, Cu, Cr, Ni, Mn, etc).

Keywords: air pollution control residue (APCr); bottom ash (BA); fly ash (FA); enhanced metal recovery (EMR); waste incinerators

check for updates

Citation: Wehrung, Q.; Bernasconi, D.; Destefanis, E.; Caviglia, C.; Curetti, N.; Di Felice, S.; Bicchi, E.; Pavese, A.; Pastero, L. Aqueous Carbonation of Waste Incineration Residues: Comparing BA, FA, and APCr Across Production Scenarios. *Minerals* **2024**, *14*, 1269. https://doi.org/10.3390/min14121269

Academic Editors: Fei Wang and Rafael Santos

Received: 17 November 2024
Revised: 5 December 2024
Accepted: 11 December 2024
Published: 13 December 2024

1. Introduction

In recent decades, mineral carbonation—also referred to as CO_2 mineralization—of industrial alkaline waste (IAW) has evolved from a promising waste management strategy into a commercially viable solution [1,2]. Accelerated Carbonation Technology (ACT) not only stabilizes these wastes but also significantly reduces CO_2 emissions, all while producing valuable byproducts for reuse [3,4]. Leading companies include Carbon8 and O.C.O Technology (UK) in the Municipal Solid Waste Incineration (MSWI) and cement sectors [5], Orbix (Belgium), Mineral Carbonation International (Australia), and RHI Magnesita in the steel and refractory products sectors [6], as well as Neustark (Switzerland), Heidelberg Materials (Germany), and Carbonaide (Finland) in the concrete sector [7]. Specifically, the wet, ex situ ACT process—also called ex situ aqueous carbonation—consists of creating a slurry to accelerate the dissolution of both CO_2 and reagents, which in turn enhances efficient carbonate precipitation. Aqueous carbonation is widely favored for its scalability, as it requires milder conditions than gas–solid carbonation and enables further intensification through additives, catalysts, process integration, alternative energy, and innovative reactor designs [8]. While the scale-up of ACT is ongoing, relevant efforts are still required to fully realize its potential in addressing key environmental challenges related to carbon capture and storage (CCS), waste management, and the circular economy at large.

In particular, the chemical and mineral heterogeneity, along with the toxicity of MSWI residues, presents a significant challenge to their widespread integration into this emerging industry [9,10]. MSWI generates three main types of alkaline solid residues: bottom ash (BA), fly ash (FA), and air pollution control residue (APCr) [11]. Their production scenarios—ranging from the initial MSW feedstocks to their collection and storage at the outlet of the incineration process—along with factors such as the waste inflow, combustion conditions, process layout and solid additives, significantly influence their physicochemical properties, which ultimately determine their suitability for ACT. Furthermore, increasing quantities of sorted MSW have led to higher production of refuse-derived fuels (RDFs), which are then incinerated. This results in BA with distinct characteristics compared to non-pretreated MSWI [12–17]. Key factors include grain sizes, mineral composition, and leachability, which all play a critical role in any carbonation process [18,19].

Figure 1 illustrates the MSWI process diagram for a typical electricity and heat cogeneration plant, highlighting the collection points for BA, FA and APCr. BA are collected beneath the incineration chamber, while FA are typically retrieved from the boiler and electrofilters [20–22]. The finer fractions of BA are both toxic and highly reactive during carbonation, thus presenting a challenge for their management but also an opportunity for potential use [23,24]. FA are defined as "the particulate matter carried over from the combustion chamber and removed from the flue gas stream prior to the addition of any type of sorbent material" [25]. If sorbent additives are used upstream, electrofilter residues should be classified as APCr. Additionally, residues gathered in the bag filters located downstream of the gas cleaning system are likewise categorized as APCr [26]. Residues from the boiler, electrostatic filters, and bag filters are either blended or maintained apart in big bags or silos by the facilities. Either lime or sodium bicarbonate are typically employed as sorbents for acid gas removal, alongside lignite powder to control dioxins and mercury emissions [27,28]. Lime plays a crucial role in forming calcium (chloro)(hydr)oxide (CCHO) phases, which are highly reactive in FA, and APCr [29]. $Ca(OH)_2$ is widely recognized as the primary driver of carbonation in BA, FA, and APCr, although in most cases, Ca-aluminates serve as the main source of calcium in BA [30–33]. The products of the acid gas removal reactions involving lime, HCl and $Cl_{2,}$ are identified as a solid solution of CaClOH and $CaCl_2{\cdot}2H_2O$ [34,35]. These compounds also play a key role as Ca providers in the carbonation of FA and APCr [36–39].

While ACT has been commercially implemented for FA and APCr by UK companies such as Carbon8 and OCO Technology, there are currently no successful industrial case studies involving BA. The most significant full-scale advancements were reported by THM University of Applied Sciences in Gießen and the Department of Geosciences at the University of Cologne [40–42]. Additional pilot-scale trials were reported by the Korea Institute of Geosciences and Mineral Resources (KIGAM) [43–45]. Despite existing valorization solutions through ACT such as lightweight aggregate, cement and geopolymer manufacturing [46–51], as well as enhanced metal recovery (EMR) processes like FLUWA and FLUREC [52], FA and APCr are still largely disposed of in landfills, including underground repositories such as salt mines [53,54], as these methods remain less widespread due to logistical challenges and technological barriers. To support the sustainable development of aggregate production from BA, FA and APCr as a viable valorization pathway, advancements are required in removing potentially toxic elements prior to manufacturing and assessing the suitability of various MSWI streams. To achieve this, a combination of EMR and ACT for advanced processing of diverse feedstocks—including both waste and naturally occurring materials—is gaining attention [55–60].

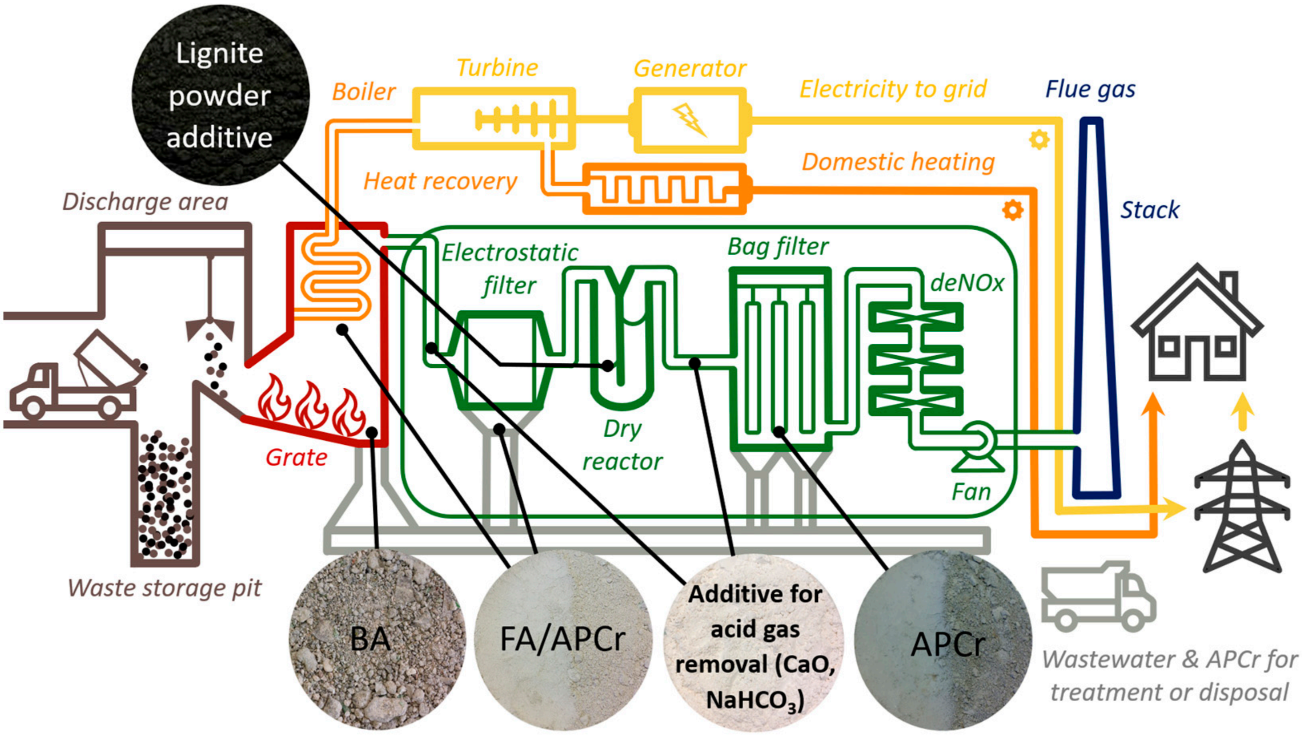

Figure 1. MSWI process diagram of a typical electricity and heat cogeneration plant, showing the collection points of the solid residues: BA, FA, APCr as well as the most common solid additives (lignite powder, lime, sodium bicarbonate). Not to scale. Note that electrofilter residues can be classified as either FA or APCr, depending on whether additives were used upstream.

In this context, the present work aims to compare the reactivity of BA, FA, and APCr toward aqueous carbonation under typical MSWI production scenarios by evaluating:

- Total CO_2 uptake, assessed through measurements of carbonation capacity, carbonation degree achieved, and resulting efficiency.
- Kinetic behaviour, evaluated by measuring the CO_2 absorption rate.
- Leachability of heavy metals (HMs), determined by analyzing HMs concentrations in the carbonated wastewater and assessing the stability of the carbonated product.

We selected five representative samples from three facilities—A, B, C, D, and E. Each sample underwent thorough physicochemical characterization to correlate its properties with performance. Relying on previous studies, regular water-washing and aqueous carbonation tests were conducted, with CO_2 bubbling as the sole variable [61]. The aim was to evaluate and compare the effectiveness of aqueous carbonation versus regular washing in the removal and stabilization of heavy metals (HMs). Carbonation tests were carried out under dynamic conditions, using high-precision gas flow sensors for continuous CO_2 flow monitoring, completing previous methods adapted to pressurized vessels [62]. A novel method, based on previous studies [63,64], was implemented to measure in situ the degree of carbonation. A novel mechanism for Cr leaching during and after BA carbonation was proposed, and its implications for designing a more sustainable management process layout were discussed.

2. Materials and Methods

2.1. Reagents

The A, C, and E samples were collected concurrently from the same French plant (plant 1), while B and D were provided by an Italian plant (plant 2) and another French plant (plant 3), respectively. Figure S1 illustrates the samples collected from Plant A, including all discarded coarse BA fractions, while Figure S2 shows the grain size distribution curve of these BA. Figure 2 illustrates the methodology used to select the samples, as well as the five chosen samples, which represent the most common MSWI residue production scenarios. $Ca(OH)_2$, used as a standard to calculate the carbonation degree achieved during the experiments, was provided by ERBApharm with a purity of 98% and a specific surface area (SSA) of 16.035 $m^2/g \pm 0.09$ ($R^2 = 0.999$). CO_2 was provided by Sapio at a purity of 99.9%. Ultrapure and degassed water were used throughout the experiments. All samples were collected a few days after generation, dried in an oven at 378 K and eventually analyzed.

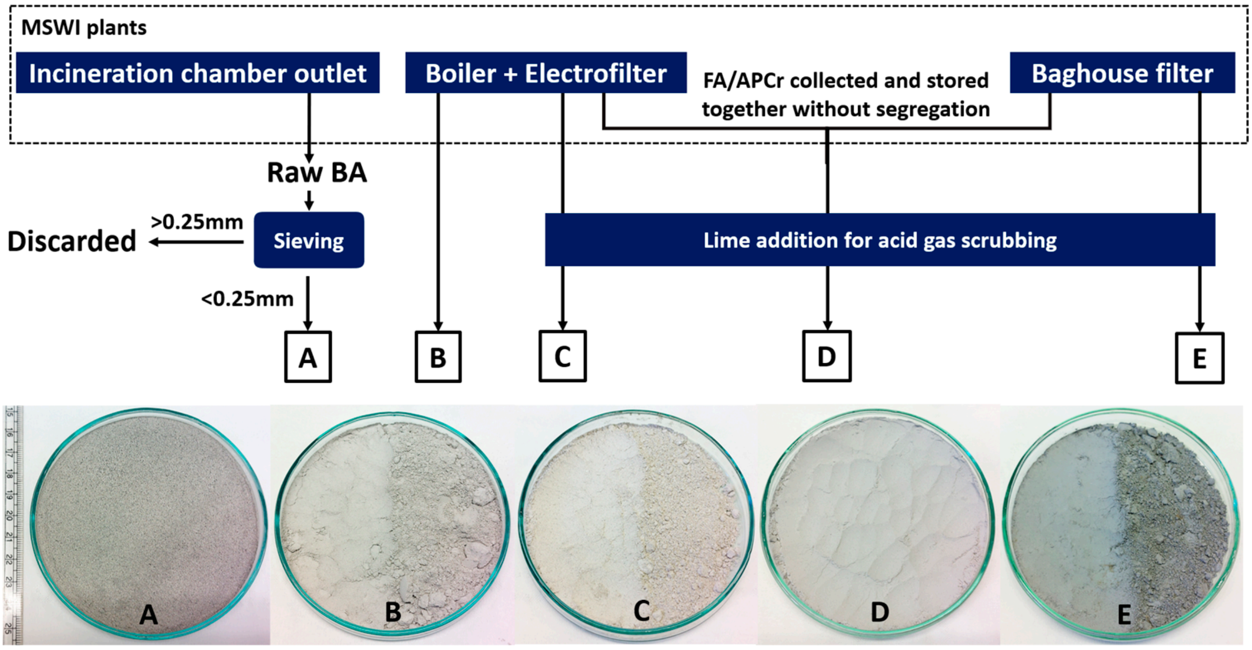

Figure 2. Methodology for selecting representative samples to assess carbonation reactivity across common MSWI residue production scenarios, highlighting the five raw selected samples for this study: (**A**): BA under 0.25 mm, (**B**): FA from boiler and electrofilter, (**C**): APCr from boiler and electrofilter, (**D**): APCr from boiler, electrofilter and bag filter, (**E**): APCr from bag filter.

The BA fraction under 0.25 mm, sample A, represents 11.15 wt.% of the total BA mass, as shown by Figures S1 and S2. This fraction was chosen for its superior specific surface area, calcium availability, and toxicity compared to coarser fractions [65]. Sample B originates from Italian plant 2 utilizing the NEUTREC® technology, which uses sodium bicarbonate ($NaHCO_3$) downstream as an additive for acid gas removal. These residues are known for their high leachability of chlorides, sulfates, fluorides, and oxyanions (e.g., from As, Cr, Sb, Se) [27,66]. The leachate typically has a pH of around 8.5, similar to $NaHCO_3$ in equilibrium with water. The APCr from plant 2 are normally processed to produce sodium hydroxide (brine) for the salt industry, by SOLVAL S.p.A. Sample C consists of boiler and electrofilter residues, while sample E is composed of APCr from the bag filter of French plant 1. In plant 1, $Ca(OH)_2$ is injected by cyclones both before the electrofilter and the bag filter. Sample D derives from French plant 3 applying a semi-dry process injecting CaO and steam for acid gas removal [67]. Sample D results from combining boiler and electrofilter ashes with the APCr from the bag filter in shared storage silos.

2.2. Experimental Procedures

Each experiment was conducted in a double-wall Pyrex reactor with a capacity of 1.5 L, a height of 16.8 cm, and a diameter of 10 cm, equipped with a thermostatic bath, as reported in previous studies [63]. The detailed experimental conditions are provided in Table 1. Each of the five samples underwent two tests: regular water washing and aqueous carbonation, with CO_2 bubbling as the sole difference. Ten experiments were therefore conducted, as listed in Table 2 with the following identifiers: A1, A2, B1, B2, C1, C2, D1, D2, E1 and E2.

Table 2 provides the experiment identifiers with their corresponding duration and liquid sample names. The methods for calculating the average CO_2 absorption rate during the aqueous carbonation experiments, the theoretical carbonation capacity, and the carbonation degree of the solid samples were developed and implemented in previous studies [63,64]. The relevant formulas are detailed in the Supplementary Information as Equations (S1)–(S6). Pure CO_2 was used at a constant partial pressure of 1.2 bar and a flow rate of 0.4 L/min. The stirrer speed was 300 rpm, with a reagent concentration of 2.5 wt.% (L/S ratio of 40), totaling 24 g of sample per experiment. The temperature was maintained at 333 K, within field-scale carbonation ranges. Reactants were combined with ultra-pure water under an Ar atmosphere. Subsequently, the suspension was poured into the reactor. The solution was stirred thoroughly for at least 10 min to ensure proper mixing of the suspension. During this time, Ar was bubbled through the solution to prevent premature carbonation caused by exposure to ambient air. Before conducting the carbonation experiments—A1, B1, C1, D1, and E1—CO_2 was flushed through the reactor to remove residual air. At t = 0, CO_2 bubbling into the reactor began. These experiments were considered completed when the gas flow sensors indicated cessation of CO_2 absorption by the solution (i.e., inlet flow = outlet flow). Subsequently, regular water-washing experiments—A2, B2, C2, D2, and E2—were carried out for a duration comparable to that of their respective aqueous carbonation counterparts. Upon completion of each experiment, 10 mL of the resulting wastewater was sampled, filtered and collected for further analysis. A portion of the solid samples was also filtered, dried, and subsequently collected for further analysis.

Table 1. Overview of the experimental parameters and their corresponding values.

Parameter	Unit	Value
Water mass	kg	1
Solid sample mass	g	25
Liquid-to-solid ratio	-	40
Pressure	bar	1.2
Temperature	K	333
CO_2 volumetric flow rate	L/min	0.4
CO_2 concentration	vol.%	100
Stirrer speed	rpm	300
Cylinder height × diameter	cm	16.8 × 10

Table 2. Experiment identifiers, durations, and corresponding liquid sample names. Each experiment includes two liquid samples: (1) washing wastewater, collected in the reactor after the experiments, and (2) leachate from the toxicity characteristic leaching procedure (TCLP) of the filtered solid residue.

Sample	Experimental Identifier		Duration	Liquid Sample Names			
	Aqueous Carbonation	Water Washing	(min)	Aqueous Carbonation WW [1]	TCLP [2]	Water Washing WW	TCLP
A	A1	A2	50	AA	AC	AB	AW
B	B1	B2	15	BA	BC	BB	BW
C	C1	C2	40	CA	CC	CB	CW
D	D1	D2	30	DA	DC	DB	DW
E	E1	E2	45	EA	EC	EB	EW

[1] The liquid sample names of this column refer to the wastewater (WW) from the corresponding experiments.
[2] The liquid sample names of this column refer to the TCLP leachates from the corresponding experiments.

2.3. Analytical Methods

The SSA of the raw samples was determined using a Micromeritics ASAP 2020 instrument, following the Brunauer–Emmett–Teller (BET) method with nitrogen adsorption at −196 °C. Prior to analysis, samples were degassed at 150 °C for 240 min. Elemental composition was measured via X-ray fluorescence (XRF) using a Rigaku Supermini200. To identify and quantify the solid-state phases, X-ray powder diffraction (XRPD) was performed with a Rigaku MiniFlex 600 benchtop diffractometer, scanning between 3° and 90° at a speed of 0.2°/min. Three separate XRPD data collections were performed on the raw APCr samples, using the Rietveld method with corundum as an internal standard for phase quantification. Surface structure and morphology were investigated using a TESCAN VEGA 3 scanning electron microscope (SEM) paired with Oxford Xplore 15 energy dispersive X-ray spectroscopy (EDS) for elemental mapping. TCLP leaching tests were conducted following the LS EN-12457 standards [68]. For ion quantification in solution, a Metrohm 883 Basic IC Plus with an 863 Compact autosampler was used in conjunction with Metrosep C/A Supp 4—250/4.0 columns, detecting cations and anions including sodium, potassium, calcium, magnesium, chloride, sulfate, and bromide. For HM detection, inductively coupled plasma mass spectrometry (ICP-MS) was employed, utilizing a Thermo Fisher iCAP-TQe system with an ASX 560 autosampler. Al, As, Cd, Cu, Co, Cr, Fe, Mn, Ni, Pb, Sb, and Zn were detected. After filtering and diluting the samples in ultrapure water, they were acidified with 0.1% nitric acid (HNO_3), and calibration was performed using five standards ranging from 1 to 50 ppm. pH levels were measured with a Hanna HI H-ORP meter, while electrical conductivity (EC) was assessed using a Mettler Toledo FiveEasy EC meter. To monitor the CO_2 flow and total uptake, a Bronkhorst modular system was used, comprising a Mass Stream controller (MFC D-6321) for flow regulation, which had a maximum capacity of 2 Ln/min and an accuracy of ±1.0% RD plus ± 0.5% FS, and a flow meter (F101E) with a maximum flow rate of 3 Ln/min and an accuracy of ± 1.0% FS. The system also included a digital interface based on the FLOW-BUS protocol, enabling diagnostics and communication via RS232. CO_2 absorption data were recorded every second throughout the experiments.

3. Results and Discussion

3.1. Physicochemical Characterization of MSWI Residues

3.1.1. Mineralogy and Chemistry

The XRPD patterns of the raw MSWI residue samples are presented in Figure 3. The SSA, the loss on ignition (LOI), the Rietveld quantification of mineral phases, and the XRF chemical composition are provided in Table 3. XRPD allowed the recognition of twenty-seven mineral phases, thus showing the relevant mineralogic heterogeneity of MSWI residues.

The most abundant minerals were CaClOH, portlandite, larnite, calcite, halite, sylvite, and anhydrite. XRF identified and quantified twenty-one oxides, with CaO leading the chemical composition in samples A, C, D, and E, at 50.2, 54.8, 76.7, and 61.4 wt.%, respectively. Using the modified Steinour equation (Equation (S4)), XRF quantification allows the calculation of the theoretical carbonation capacity φ (g CO_2/kg MSWI residue) of the samples. The φ values for samples A, B, C, D, and E were 389.5, 64.4, 392.9, 524.6 and 443.1 g CO_2/kg, respectively. However, these values do not account for the CO_2 amount already present as carbonate, which can be derived from the Rietveld analysis and should be subtracted for accuracy. Thus, the adjusted φ values are 365.3, 56, 392.9, 458.2 and 425.3 g CO_2/kg, respectively.

Sample A contains a low proportion of CCHO, with only 0.8 wt.% $Ca(OH)_2$. Most of the calcium is bound to Ca-Al hydroxides, specifically hydrocalumite (Hcl) and katoite (Kto). Hcl is known to precipitate from $Ca(OH)_2$ and $Al(OH)_3$ in water, in competition with the formation of Kto [69]. Hcl is known to slowly transform into Kto in alkaline solutions, where Kto is thermodynamically more stable and less soluble [70]. Jiménez [71] proposed that Cl-bearing Hcl may decompose thermally in mayenite ($Ca_{12}Al_{14}O_{33}$), CaClOH and CaO. Note that ettringite (Ett) was not detected in sample A, even though it is one of the most common Ca-Al hydroxides found in BA and specifically bears sulfates [72–74].

Sample B lacks CCHO and has the lowest CaO concentration but is highly enriched in Na_2O, K_2O, and Cl, reflecting the use of $NaHCO_3$ instead of lime. Its elevated ZnO, Sb_2O_3, and PbO levels indicate strong EMR potential.

Sample C is rich in CCHO and contains notable Ca- and Mg-bearing silicates. Its HM content is lower than sample A but includes significant Fe_2O_3, TiO_2, and ZnO, with Sb_2O_3 also detected. Alkali-chloride levels are typical of boiler/electrofilter residues.

Sample D exhibits the highest CCHO proportion. Sulfur is present in the form of the sulfite mineral hannebachite. This sample also contains the highest proportion of calcite, consistent with the use of a semi-dry process involving CaO and steam, which promotes early carbonation from flue gas. Chemically, sample D has the highest CaO content and shows no potential for EMR. Notably, alternative alkali oxides are nearly absent compared to the other samples, with only trace amounts of Na_2O and K_2O. Additionally, this sample has the highest crystalline content.

Sample E features a high proportion of CCHO. The total Cl content is elevated, consistent with the presence of CaClOH, halite, and sylvite. This sample also has the highest amorphous content and the lowest HMs proportions. Interestingly, the comparison of hazardous trace metal content between samples A, C, and E produced results consistent with Zhao [75], who classified the volatility of seven metals in the following order: Cd, As > Ni, Zn > Pb > Cr, Cu. Consequently, BA contains higher proportions of Cr and Cu, while boiler and bag filter residues have comparatively higher concentrations of Pb and Zn. Sample E has the highest SSA, indicating a higher proportion of small and light particles, consistent with pure bag filter residue located downstream of the gas cleaning system.

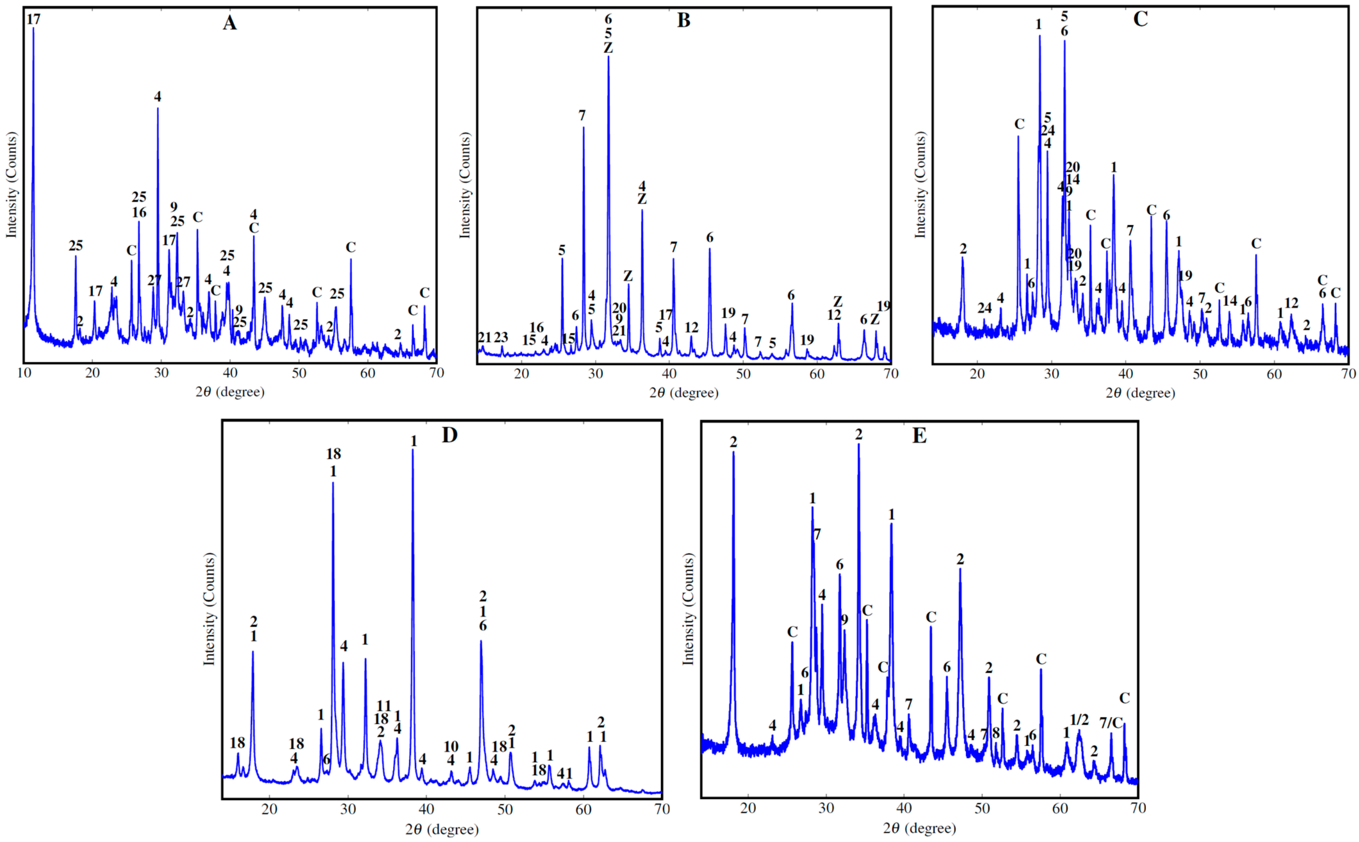

Figure 3. XRPD patterns for (**A**) sample A (**B**) sample B (**C**) sample C (**D**) sample D (**E**) sample E. Legend for the XRPD mineral phases: C: Corundum (standard), Z: ZnO (standard) 1: CaClOH, 2: portlandite, 3: magnesite, 4: calcite, 5: anhydrite, 6: halite, 7: sylvite, 8: hatrurite, 9: larnite, 10: sinjarite, 11: $CaCl_2{\cdot}4H_2O$, 12: periclase, 13: melilite, 14: lime, 15: quartz, 16: cristobalite, 17: hydrocalumite, 18: hannebachite, 19: ilmenite/perovskite, 20: merwinite, 21: bassanite, 22: singenite, 23: K-tetrachlorozincate, 24: gehlenite, 25: katoite, 26: hydroxiapatite, akermanite: 27, mullite: 28.

Table 3. BET SSA (m^2/g), LOI (wt.%), Rietveld mineral quantification (wt.%), and XRF chemical composition of the samples studied (wt.% of oxides). Chloride (Cl) is also included, expressed in atomic form. Note that the chemical composition data do not include LOI.

		A	**B**	**C**	**D**	**E**
SSA	(m^2/g)	4.182	3.125	3.955	13.487	26.844
LOI	wt.%	21.8	23.3	12.5	20.5	38.6
Phase name	Formula					
CaClOH	CaClOH	-	-	14.3	44.3	20.8
Portlandite	$Ca(OH)_2$	0.8	-	2.1	7.2	9.8
Lime	CaO	-	-	1.7	-	-
Sinjarite	$CaCl_2{\cdot}2H_2O$	-	-	-	0.9	-
$CaCl_2{\cdot}4H_2O$	$CaCl_2{\cdot}4H_2O$	-	-	-	0.6	-
Periclase	MgO	-	1.4	0.8	-	-
Larnite	Ca_2SiO_4	3.7	0.7	6.7	-	1.5
Hatrurite	Ca_3SiO_5	-	-	-	-	1.8
Akermanite	$Ca_2MgSi_2O_7$	1.5	-	-	-	-
Melilite	$Ca_2(Al,Mg)(Al,Si)_2O_7$	-	1.3	-	-	-
Gehlenite	$Ca_2Al_2SiO_7$	-	-	3	-	-
Merwinite	$Ca_3Mg(SiO_4)_2$	-	0.8	2.4	-	-
Magnesite	$MgCO_3$	-	-	-	-	0.3
Calcite	$CaCO_3$	5.5	1.9	-	15.1	3.7
Quartz	SiO_2	1.6	0.6	-	-	-
Cristobalite	SiO_2	0.5	0.2	-	-	-
Halite	NaCl	-	25.1	6.4	0.7	4.1
Hydrocalumite	$Ca_2Al(OH)_6(Cl,OH){\cdot}2H_2O$	14.2	0.5	-	-	-
Katoite	$Ca_3Al_2(OH)_{12}$	12.2	-	-	-	-
Calcium Alum. Nitrate	$Ca_3Al_2(NO_3)_{12}$	2.8	-	-	-	-
Hydroxiapatite	$Ca_5(PO_4)_3OH$	4.0	-	-	-	-
Archerite	$KHPO_4$	0.1	--	-	-	-
Anhydrite	$CaSO_4$	-	11.3	4.9	-	1.2
Bassanite	$CaSO_4{\cdot}0.5H_2O$	-	4.5	1.8	-	-
Hannebachite	$CaSO_3{\cdot}0.5H_2O$	-	-	-	19.1	-
Sylvite	KCl	-	12.1	4.9	-	1.3
Ilmenite/Perovskite	$(Fe,Ca)TiO_3$	1.4	0.6	1.3	-	-
K-tetrachlorozincate	K_2ZnCl_4	-	0.5	-	-	-
Amorphous		51.7	38.2	41.8	12.0	55.5
	Oxide					
	Na_2O	1.28	14.72	5.36	0.1	4.35
	MgO	2.45	1.79	0.81	0.56	0.54
	Al_2O_3	18.67	1.23	1.83	0.18	0.39
	SiO_2	12.08	5.05	3.89	0.49	1.86
	P_2O_5	2.81	0.95	0.86	0.07	0.08
	SO_3	2.53	12.33	7.41	15.08	8.04
	Cl	2.40	24.21	15.14	5.28	19.49
	K_2O	0.75	14.09	4.99	0.46	2.49
	CaO	50.21	15.10	54.80	76.70	61.40
	TiO_2	1.78	0.58	1.25	-	-
	Cr_2O_3	0.09	0.08	0.06	-	-
	MnO	0.14	0.06	0.08	0.04	0.05
	Fe_2O_3	3.17	1.05	1.23	0.63	0.54
	NiO	0.02	0.01	0.01	-	-
	CuO	0.25	0.23	0.11	-	0.03
	ZnO	0.85	6.38	1.32	0.16	0.45
	SrO	0.10	0.03	0.08	0.07	0.04
	ZrO_2	0.02	0.01	0.02	-	-
	Ag_2O	0.16	-	-	-	-
	Sb_2O_3	-	0.31	0.13	-	-
	BaO	0.18	0.06	0.12	-	-
	PbO	0.03	0.83	0.16	0.02	-

3.1.2. Microstructure

Figure 4 illustrates the morphology of the particles in sample A. Layered Ca-Al particles, densely dispersed across the sample, were the predominant morphology detected. Similar particles were observed by Moon [76] and identified as Kto whereas Jiménez [71] ascribed them to Hcl. As Hcl and Kto exhibit similar morphology, such phases are distinguishable from one another by their chemical composition. Notably, Hcl contains a significant amount of Cl, approximately 12.6 wt.%, while Kto does not. EDS scans of the layered Ca-Al particles reveal Cl concentrations ranging from 0 to 7.2 wt.%, suggesting that Hcl and Kto particles were packed together. Additional Ca-Al morphologies were identified, as illustrated by the botryoidal particle in Figure 4C. Apatite was also detected, consistently with the XRPD results. Highly heterogeneous particles, mainly composed of alkali chlorides and molten glasses, were found. Finally, the XRPD and SEM-EDS patterns of sample A's magnetic fraction from dry extraction, as shown in Figure S3, indicate the presence of iron oxides, including visible crystals of hematite and magnetite.

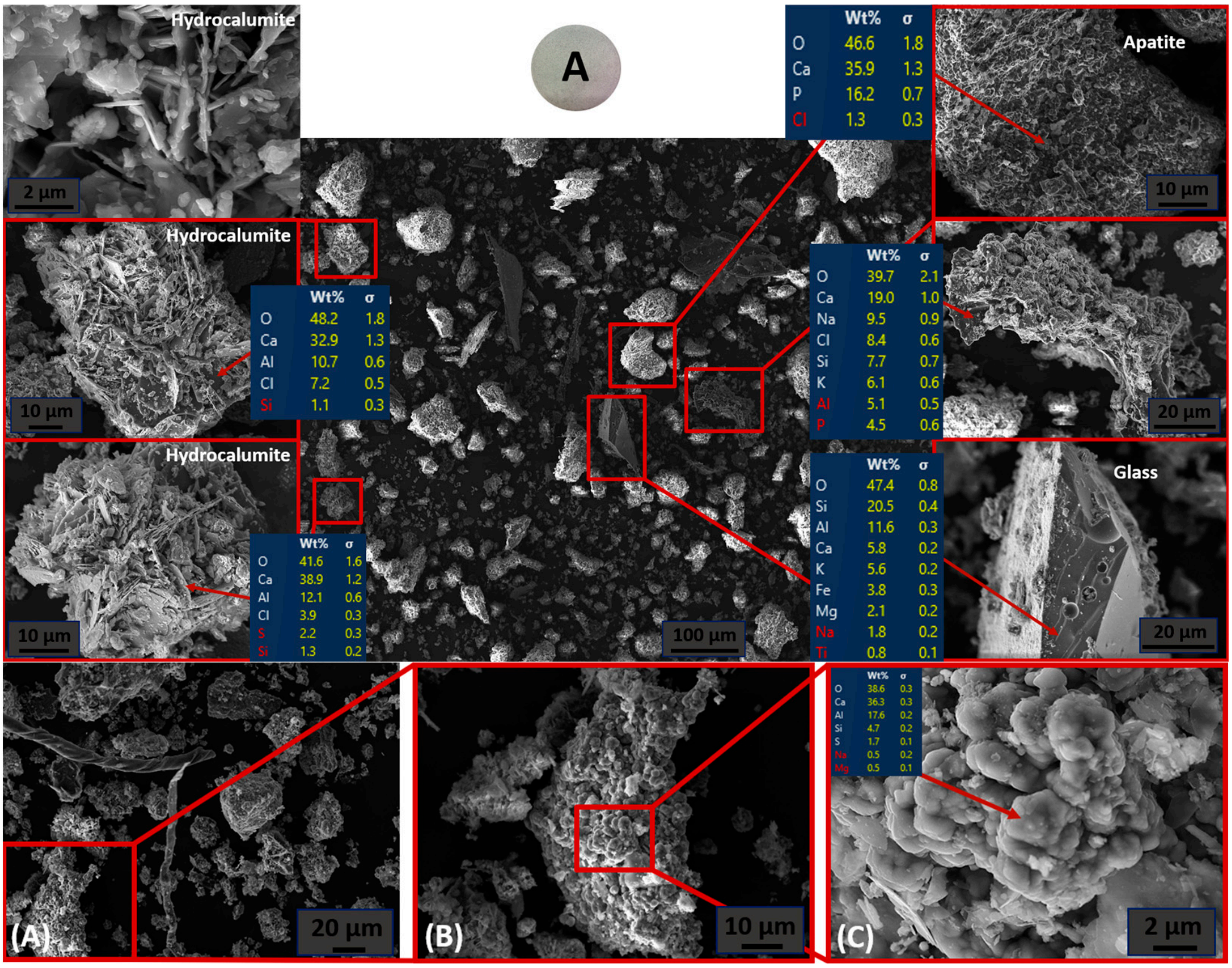

Figure 4. SEM-EDS patterns of characteristic phases and minerals observed in sample A. (**A**–**C**) illustrate a zoom-in from the sample's bulk matrix to a Ca-Al particle exhibiting a botryoidal morphology.

Figure 5 depicts the typical SEM view of sample B. SEM-EDS patterns confirmed the prevalence of alkali chlorides and Zn-containing phases, along with the lower Ca concentration quantified by XRPD and XRF. A large proportion of nanoparticles were mixed or adsorbed onto glass spheres and large silicate single crystals.

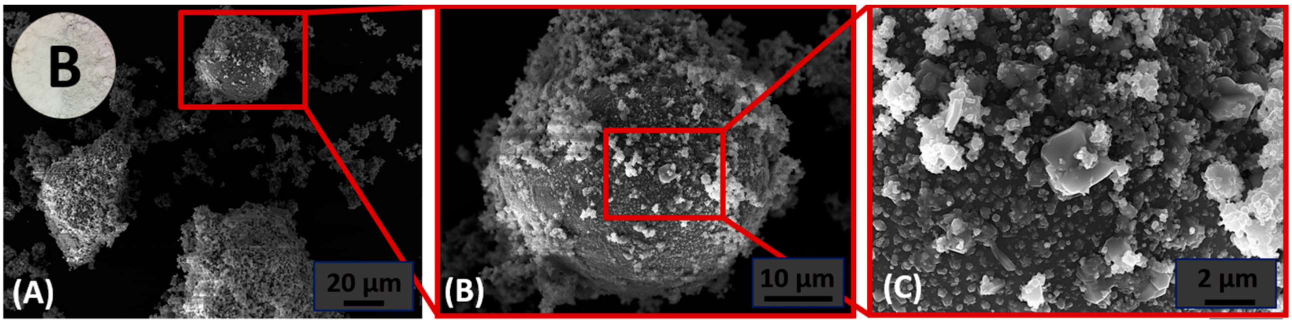

Figure 5. SEM-EDS patterns of characteristic phases and minerals observed in sample B. (**A**–**C**) illustrate a zoom-in from the sample's bulk matrix to the surface of a glass sphere.

Figure 6 presents a typical SEM view of sample C, highlighting key morphological features. Notably, distinct CCHO particles with a sheared morphology were concentrated in the sample. Glass spheres and iron oxides, common phases in boiler and electrostatic filter residues, were also observed. Additionally, cubic crystals of sodium chloride and unreacted lime particles were identified.

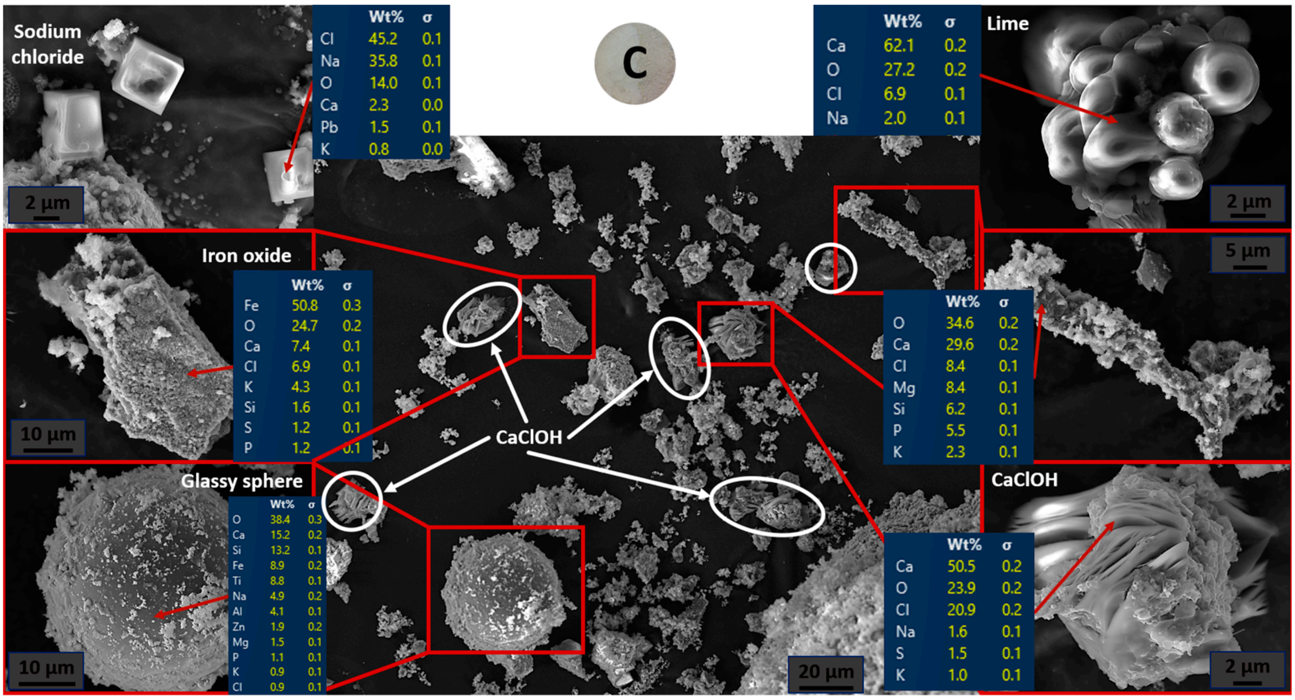

	Wt%	σ
Cl	45.2	0.1
Na	35.8	0.1
O	14.0	0.1
Ca	2.3	0.0
Pb	1.5	0.1
K	0.8	0.0

	Wt%	σ
Ca	62.1	0.2
O	27.2	0.2
Cl	6.9	0.1
Na	2.0	0.1

	Wt%	σ
Fe	50.8	0.3
O	24.7	0.2
Ca	7.4	0.1
Cl	6.9	0.1
K	4.3	0.1
Si	1.6	0.1
S	1.2	0.1
P	1.2	0.1

	Wt%	σ
O	34.6	0.2
Ca	29.6	0.2
Cl	8.4	0.1
Mg	8.4	0.1
Si	6.2	0.1
P	5.5	0.1
K	2.3	0.1

	Wt%	σ
O	38.4	0.3
Ca	15.2	0.2
Si	13.2	0.1
Fe	8.9	0.2
Ti	8.8	0.1
Na	4.9	0.2
Al	4.1	0.1
Zn	1.9	0.2
Mg	1.5	0.1
P	1.1	0.1
K	0.9	0.1
Cl	0.9	0.1

	Wt%	σ
Ca	50.5	0.2
O	23.9	0.2
Cl	20.9	0.2
Na	1.6	0.1
S	1.5	0.1
K	1.0	0.1

Figure 6. SEM-EDS patterns of characteristic phases and minerals observed in sample C.

Figure 7 illustrates the typical features observed in sample D, revealing a relatively homogeneous bulk matrix. Trigonal prismatic portlandite and trigonal calcite crystals are clearly visible in Figure 7C,E,F,I. Additionally, sheared structures of CaClOH, similar to those found in sample C, are densely concentrated, consistent with the 44.3 wt.% of CaClOH in this sample.

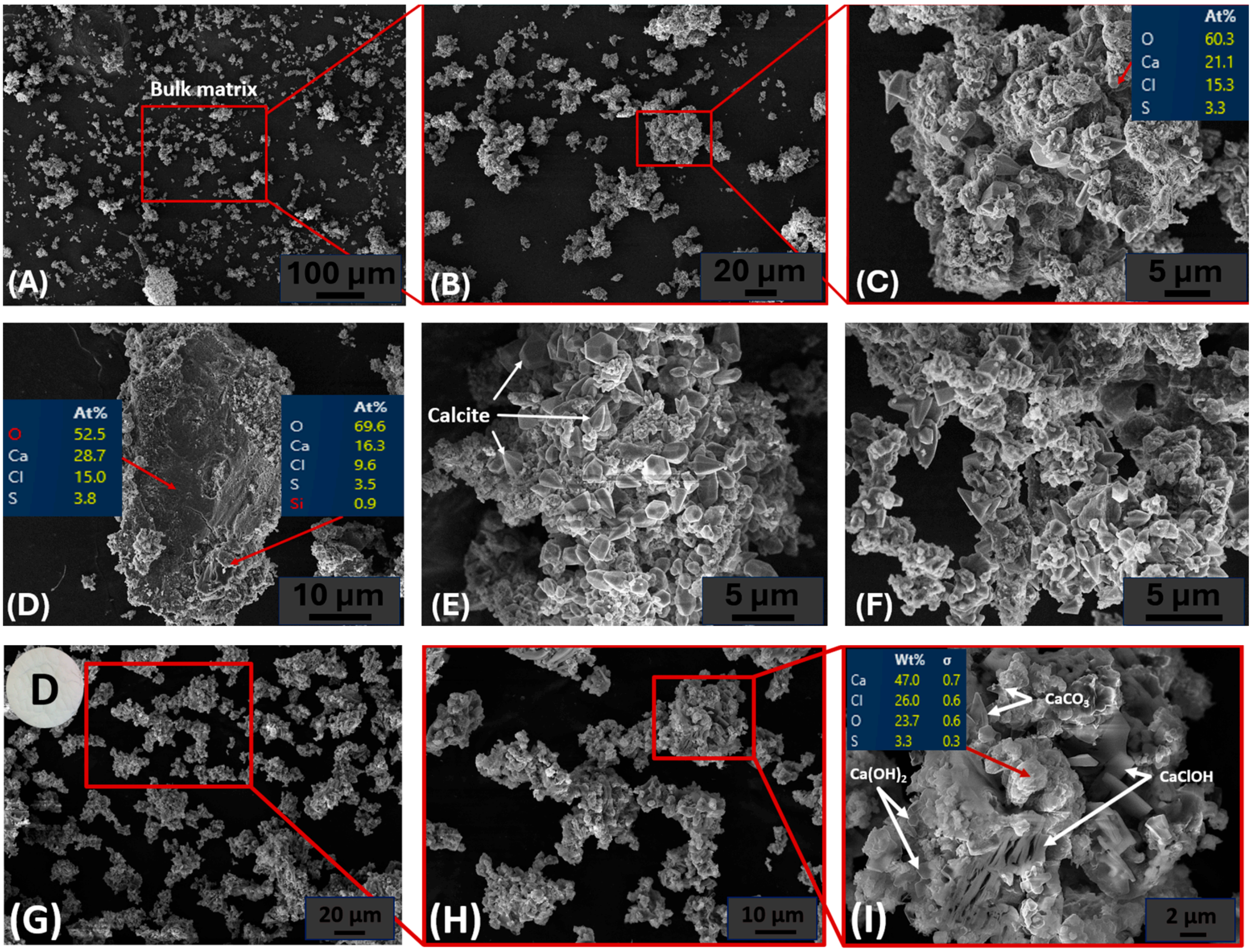

Figure 7. SEM-EDS patterns of characteristic phases and minerals observed in sample D. (**A**–**C**,**G**–**I**) illustrate a zoom-in from the sample's bulk matrix to typical particle aggregates. (**C**,**E**,**F**,**I**) show aggregates with well-grown trigonal calcite crystals. Characteristic CaClOH sheared morphology is visible in (**I**). (**D**) depicts the compact CCHO structure, with its surface free of nanoparticle adsorption.

Figure 8A–C highlight the predominant bulk matrix in sample E, consisting of a heterogeneous mixture of irregularly shaped micro- and nanosized particle aggregates. This phase exhibits significant variability in chemical composition and morphology, primarily comprising CCHO phases. Similar to samples C and D, sample E contains sheared CCHO particles, though they are less abundant and attributed to CaClOH (Figure 8E). Particles featuring significant amounts of S, Mg, K, Fe, and Al are also observed. Additionally, micrometer-sized NaCl particles are dispersed throughout the sample (Figure 8C,D). Furthermore, Figure 8F illustrates a Ca-silicate likely composed of larnite, alongside adjacent bulk matrix particles.

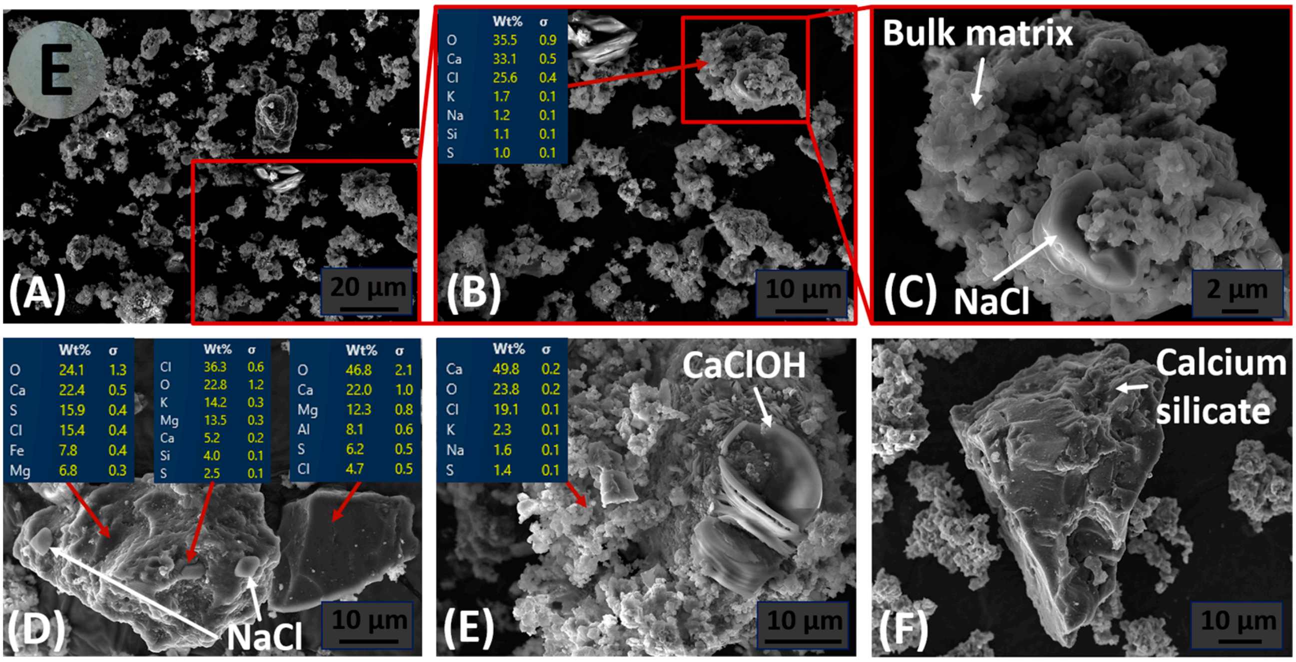

Figure 8. SEM-EDS patterns of characteristic phases and minerals observed in sample E. (**A**–**C**) illustrate a zoom-in from the sample's bulk matrix to a typical aggregate composed of heterogeneous, CaClOH-rich nanoparticles, along with a NaCl microcrystal. (**D**) shows slag particles rich in Mg, S, K, Ca, Cl, Fe, and Al, along with NaCl microcrystals. (**E**) displays a typical aggregate with characteristic CaClOH sheared morphology. (**F**) depictss a Ca-silicate, likely larnite.

3.2. Reactivity to Aqueous Carbonation of MSWI Residues

3.2.1. Theoretical Background

In MSWI residues, the most reactive minerals are calcium (chloro)(hydr)oxides, including lime, portlandite and sinjarite ($CaCl_2{\cdot}2H_2O$) [77]. Other reactive minerals include calcium silicates such as larnite and hatrurite, as well as magnesium (hydr)oxides like periclase or brucite. In BA, calcium aluminates such as Hcl, Kto, mayenite and ettringite can be the main Ca-providing minerals for carbonation [78,79]. The stoichiometric carbonation capacity (gCO_2/kg) reported for 1 kg of MSWI residue, based on free CaO, $Ca(OH)_2$, CaClOH, $CaCl_2{\cdot}2H_2O$, Ca_2SiO_4, Ca_3SiO_5, MgO and $Mg(OH)_2$, $Ca_2Al(OH)_6Cl{\cdot}2H_2O$, $Ca_3Al_2(OH)_{12}$ and $Ca_{12}Al_{14}O_{33}$ content in MSWI residues, is shown in Figure 9. The x-axis represents the corresponding theoretical relative mass concentration (%) of these minerals in the MSWI residues. Thus, the carbonation capacity of MSWI residues and other alkaline waste can typically range from 0 to 400 gCO_2/kg, depending on the Ca and Mg content that is not already bound to carbonates, sulfates, or phosphates [80]. The overall carbonation reactions involving these major Ca/Mg-bearing reactive minerals present in MSWI residue systems are listed in Table 4.

Table 4. Carbonation reactions involving major Ca/Mg-bearing reactive minerals in MSWI residues.

Mineral	**Equation of Carbonation**
Quicklime	$CaO(s) + CO_2(g) = CaCO_3(s)$
Portlandite	$Ca(OH)_2(s) + CO_2(g) = CaCO_3(s) + H_2O(l)$
Calcium chlorohydroxide	$CaClOH(s) + NaOH + CO_2(g) = CaCO_3(s) + NaCl(aq) + H_2O(l)$
Calcium chloride hydrate	$CaCl_2{\cdot}xH_2O(s) + 2NaOH + CO_2(g) = CaCO_3(s) + 2NaCl + (x + 1)H_2O(l)$
Hatrurite	$Ca_3SiO_5 + 3CO_2(g) = 3CaCO_3(s) + SiO_2(s)$
Larnite	$Ca_2SiO_4 + 2CO_2(g) = 2CaCO_3(s) + SiO_2(s)$
Periclase	$MgO + CO_2(g) + xH_2O = MgCO_3{\cdot}xH_2O(s)$
Brucite	$Mg(OH)_2(s) + CO_2(g) + xH_2O = MgCO_3{\cdot}xH_2O(s) + H_2O(l)$
Hydrocalumite	$2[Ca_2Al(OH)_6Cl{\cdot}2H_2O] + 3CO_2(g) = 3CaCO_3(s) + Al_2O_3{\cdot}xH_2O(s) + CaCl_2(aq) + (10 - x)H_2O(l)$
Katoite	$Ca_3Al_2(OH)_{12}(s) + 3CO_2(g) = 3CaCO_3(s) + 2Al(OH)_3(s) + 3H_2O(l)$
Mayenite	$Ca_{12}Al_{14}O_{33}(s) + 12CO_2(g) + 21H_2O(l) = 12CaCO_3(s) + 14Al(OH)_3(s)$
Ettringite	$Ca_6Al_2(SO_4)_3(OH)_{12}{\cdot}26H_2O(s) + 3CO_2(g) = 3CaCO_3(s) + 3[CaSO_4{\cdot}2H_2O](s) + Al_2O_3{\cdot}xH_2O(s) + (26 - x)H_2O(l)$

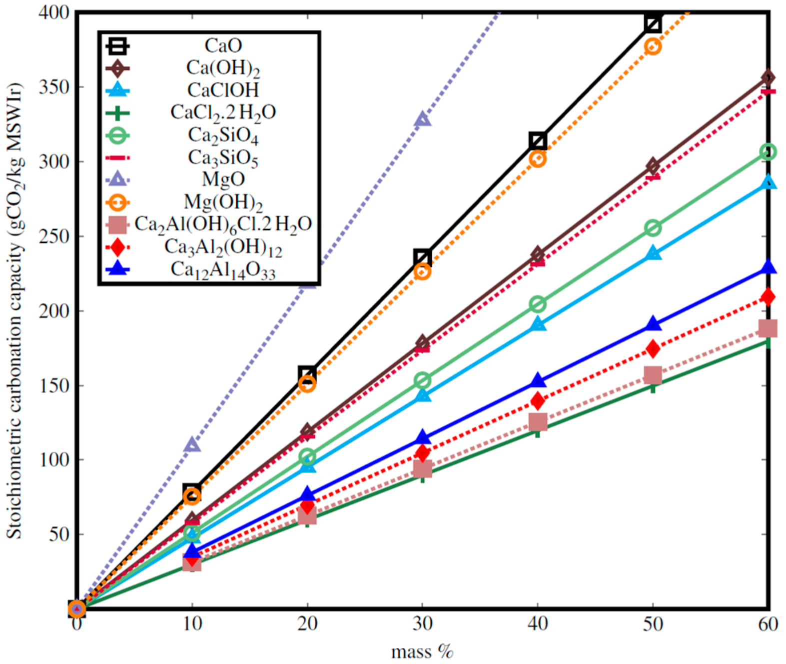

Figure 9. Stoichiometric carbonation capacity (gCO$_2$/kg) reported for 1 kg of FA/APCr, based on free CaO, Ca(OH)$_2$, CaCl$_2$·2H$_2$O, Ca$_2$SiO$_4$, Ca$_3$SiO$_5$, MgO, Mg(OH)$_2$, Ca$_2$Al(OH)$_6$Cl·2H$_2$O, Ca$_3$Al$_2$(OH)$_{12}$ and Ca$_{12}$Al$_{14}$O$_{33}$ content, as calculated according to the equations listed in Table 4.

3.2.2. CO$_2$ Absorption Rate and Total Uptake

Table 5 presents the weight loss during carbonation and water-washing experiments, reflecting the removal of soluble salts (weight loss) and the uptake of CO$_2$ (weight gain). As anticipated, the samples A1–A2 exhibited minimal weight loss (2.6–5.4 wt.%), attributed to the absence of significant soluble sulfate and chloride phases. In contrast, samples C1–C2 showed higher weight losses (21.8–25.8 wt.%), which correlate with its substantial chloride content. Samples E1–E2 also demonstrated considerable weight loss (13.8–27.8 wt.%); however, the loss was lower during carbonation, likely due to the CO$_2$ uptake. Samples B1–B2 experienced the highest weight loss (51.4–52.2 wt.%), consistent with its elevated Na-/K-chloride and sulfate content. Finally, samples D1–D2 also exhibited significant weight loss (34.2–28.4 wt.%), aligning with its high Ca-chloride content.

Table 5. Weight loss (%) of samples during carbonation and water-washing experiments.

Exp. Identifiers	**A1**	**B1**	**C1**	**D1**	**E1**	**A2**	**B2**	**C2**	**D2**	**E2**
Weight loss (%)	2.6	52.2	25.8	34.2	13.8	5.4	51.4	21.8	28.4	27.8

Figure 10 illustrates the CO$_2$ absorption rate patterns $\eta(t)$ of the five samples. Table 6 reports the carbonation performances in terms of absorption rate $\overline{\eta}(t)$, degree of carbonation achieved ω (g CO$_2$/kg), and carbonation efficiency ε (%), calculated using the carbonation capacity φ. The detailed formulas for $\eta(t), \overline{\eta}(t), \omega, \varphi, \varepsilon$ are provided in Equations (S1)–(S6). Note that it is recognized in the literature that the Steinour equation tends to overestimate the carbonation capacities of studied materials, resulting in low apparent carbonation efficiency [81].

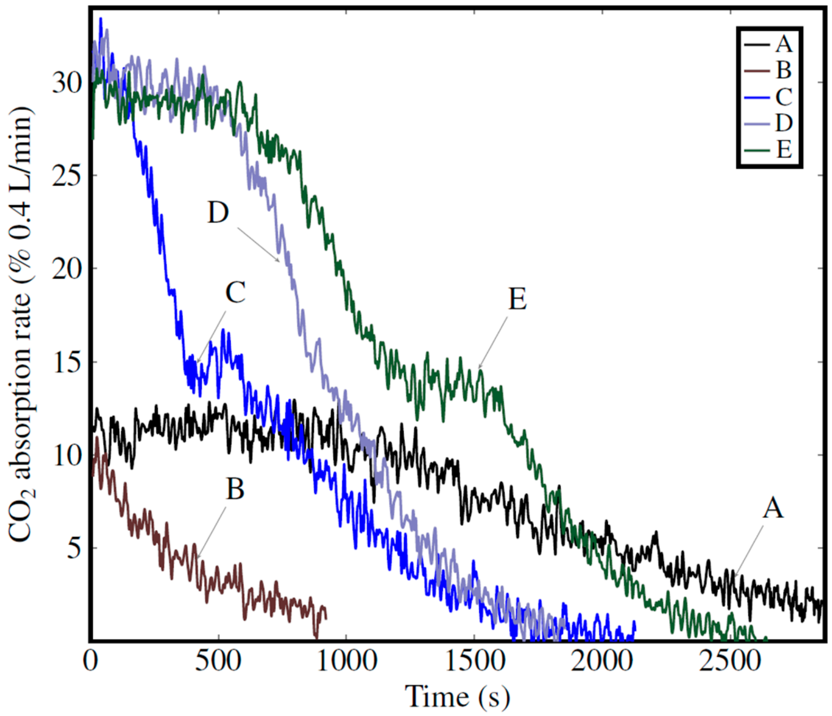

Figure 10. Comparison of CO_2 absorption rate patterns as a function of time for the samples studied (exp. identifiers: A1, B1, C1, D1, E1).

Table 6. Average absorption rate $\overline{\eta}(t)$ with standard deviation σ, duration of the carbonation phase, volumetric CO_2 uptake V_{CO2} (L), degree of carbonation achieved ω (gCO_2/kg), theoretical carbonation capacity φ (gCO_2/kg), and carbonation efficiency (%) for the aqueous carbonation.

	Unit	A	B	C	D	E
Exp. Identifiers		**A1**	**B1**	**C1**	**D1**	**E1**
$\overline{\eta}(t)$	%	10.8	0	19.9	24.7	22.3
σ	%	3.7	0	8.5	7.8	7.7
Duration	s	1455	0	725	1050	1672
V_{CO2}	L	1.05	0	0.96	1.73	2.42
ω	gCO_2/kg	101.1	0	93	167	244.5
φ	gCO_2/kg	365.3	56	392.9	458.2	425.3
ε	%	27.7	0	23.7	36.5	57.5

Samples C, D, and E exhibit similar kinetic behaviour, as indicated by the common trends in their $\eta(t)$ patterns and $\overline{\eta}(t)$ values of 29.9%, 24.7% and 23.3%, respectively. This aligns with the high CCHO content and the $Ca(OH)_2$ aqueous carbonation $\eta(t)$ patterns observed in previous studies [63]. Note that $\eta(t)$ can be easily increased by using a sparger or other static gas–liquid mixers, which produce smaller CO_2 bubbles entering the suspension [82,83]. Additionally, carbonation degrees of 93, 167 and 244.5 gCO_2/kg, with corresponding efficiencies of 23.7%, 36.4% and 57.5% were achieved for these samples, respectively. Sample E achieved the highest CO_2 carbonation degree of 244.5 gCO_2/kg, consistent with its origin from a bag filter where lime sorbent was used upstream. By comparison, sample D achieved $\eta(t)$ values smaller than expected, primarily due to calcium being retained in water due to two factors: the high solubility of calcium chloride phases and the low concentrations of alternative alkali oxides, which limited their ability to bind with chloride ions instead of calcium. Indeed, Na_2O and K_2O concentrations in sample D were significantly lower than in any other sample, at 0.098 wt.% and 0.455 wt.%, respectively. This suggests that the wastewater from carbonation experiment D1 could be re-carbonated with an alkali-hydroxide (NaOH) to precipitate nearly pure $CaCO_3$ and co-precipitate

HMs. These findings indicate that the reactivity of samples C, D and E makes them prime candidates for ACT. In contrast, sample B exhibited minimal reactivity to carbonation, and chemical data suggest its better suitability for FLUWA-FLUREC processes [84].

On the other hand, sample A displays a slower absorption rate, with an average $\overline{\eta}(t)$ value of 12.85%. The slower kinetic behaviour of BA compared to APCr was previously noted by Baciocchi [31]. Indeed, Ca-aluminates dissolve more slowly than CCHO, which results in slower CO_2 absorption rates. However, the calculated degree of carbonation achieved is still significant, at 101.1 gCO_2/kg, corresponding to an efficiency of 27.7%. Notably, the ω value closely matches the theoretical carbonation capacity based on the Rietveld quantification of calcium aluminates (90.4 gCO_2/kg), portlandite and larnite (23.6 gCO_2/kg), totaling 114.1 gCO_2/kg. These results strongly support that Ca-aluminates, primarily Hcl and Kto, are the main drivers of carbonation in BA. This value is about three times higher than commonly reported for BA in the literature, which is normally in the range of 25–45 gCO_2/kg [85,86]. However, using the fine BA fraction (<150 µm), Baciocchi [31] also reported a significant 14% CO_2 uptake driven by the carbonation of Hcl and $Ca(OH)_2$.

In BA, the leachability intensely increases with decreasing particle size [87]. Additionally, smaller particle sizes are associated with higher calcium content [88,89]. This contributes to increasing both the ecotoxicity and reactivity of fine BA fractions during carbonation. Thus, the finer BA fractions are both a challenge and an opportunity, given that separating them from the bulk BA for carbonation could significantly reduce the leachability of the bulk fraction and help mitigate CO_2 emissions. According to our data and the literature, the fraction of BA particles under 250 µm accounts for approximately 12 wt.% [90], which represents about 5 kt of material annually for a plant processing 200,000 tons of MSW per year. On a larger scale, this could amount to approximately 350 kt in a country like France. Considering an effective carbonation capacity comparable to that achieved in the present study, this amounts to an emission reduction potential of 36,000 tCO_2. The amount suitable for ACT could be even larger, as coarser fractions can adsorb fine particles and have been shown to contain Ca-aluminates, which may result in significant reactivity. The ideal granulometry for BA selection in ACT might exceed 0.5 mm, depending on the composition of specific BA streams, the overall BA processing layout, and how the carbonated material will be repurposed.

Finally, the amount of CO_2 absorbed by sample B, if any, is not quantifiable. The brief decreasing pattern corresponds only to CO_2 dissolving in water up to saturation, as demonstrated by previous studies [63]. The values of ω and ε were therefore approximated to be 0.

3.2.3. Mineralogy Changes in Carbonated and Washed Samples

Figure 11 shows the XRPD patterns of the carbonated and washed samples. Calcite was the only crystalline phase identified in the carbonated sample A, while Hcl and Kto remained present in the washed sample. Um [91] also compared the efficiency of carbonation with water washing, focusing on Cl removal in BA. They noted that Hcl, ettringite, and sodalite are the main insoluble Cl-containing phases, which decompose only in the presence of CO_2. Aluminum reprecipitates as amorphous Al-oxides [45]. The carbonated sample C produced both calcite and anhydrite, whereas calcite, portlandite, hydroxyapatite, and merwinite remained in the washed sample. The low solubility of portlandite at 333 K, combined with the dissolution of the CaClOH phase and reprecipitation as $Ca(OH)_2$, explains its consistent presence in the washed samples C2, D2, E2. In the carbonated sample E, only calcite was detected, whereas water washing resulted in portlandite, calcite, larnite, and mullite. As expected, the carbonated (B1) and washed (B2) samples exhibited nearly identical patterns. The main difference for sample B was a reduction in the intensity of the Hcl peak after carbonation, resulting in a slight increase in the calcite intensity peaks. Anhydrite, quartz, periclase, and even halite persisted in both cases. Finally, the carbonated sample D1 produced both calcite and hannebachite, while the washed sample also contained portlandite.

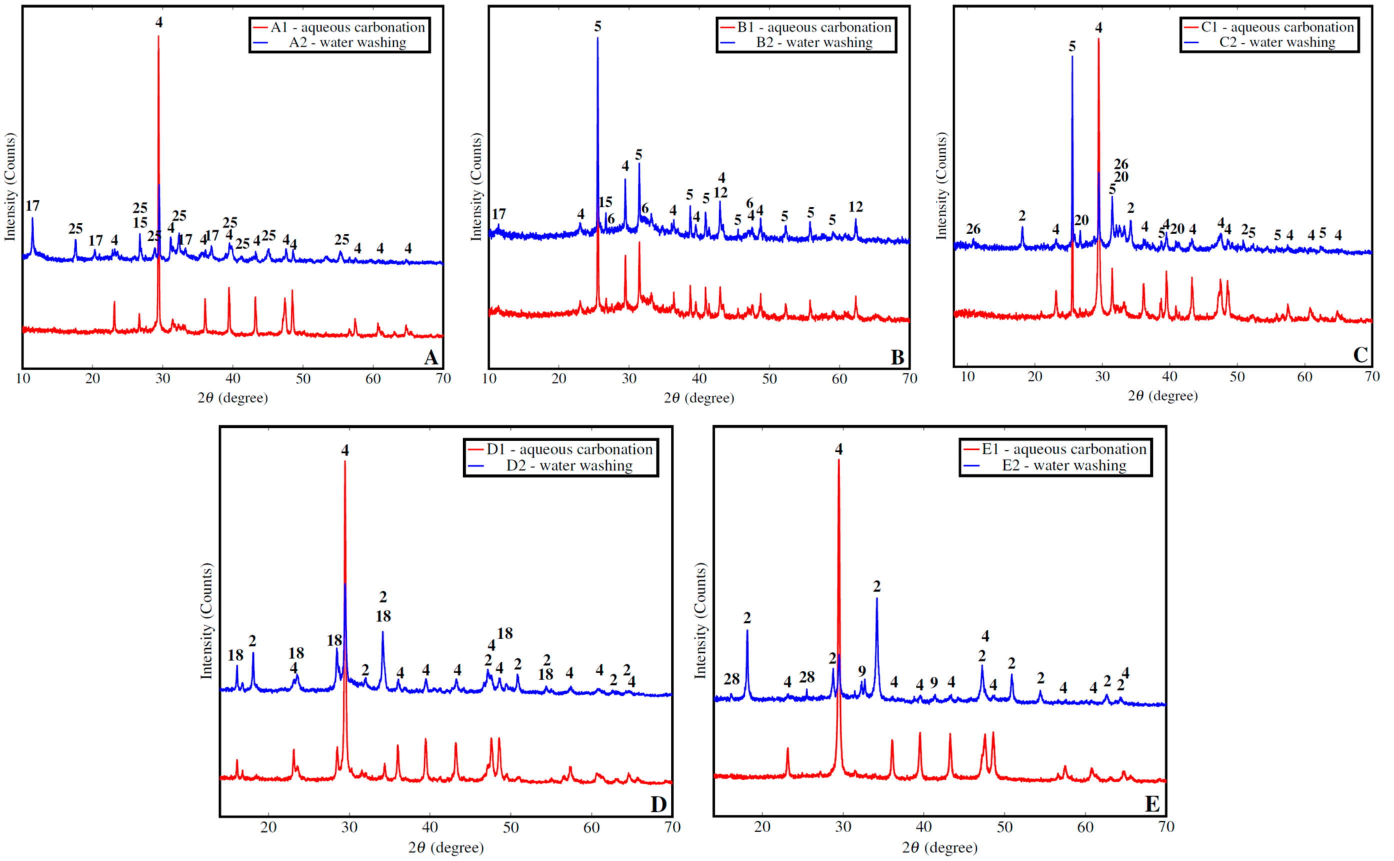

Figure 11. XRPD patterns for (**A**) sample A (**B**) sample B (**C**) sample C (**D**) sample D (**E**) sample E. Legend for the XRPD mineral phases: 2: Portlandite, 4: Calcite, 5: Anhydrite, 6: Halite, 9: Larnite, 10: Sinjarite, 12: Periclase, 15: Quartz, 17: Hydrocalumite, 18: Hannebachite, 20: Merwinite, 25: Katoite, 28: Mullite. The nomenclature used in the XRPD legend of Figure 3 was maintained for consistency.

3.2.4. HMs Leaching During and After Carbonation

Table 7 and Figure 12 present the EC/pH and HM concentrations from the TCLP analysis of raw samples, carbonated samples, and wastewater from the aqueous carbonation and water-washing experiments. Table S1 provides the physicochemical properties and the respective leaching limit values pf HMs for the use of recycled waste in France, Italy, and Germany. Detailed concentrations are reported in Table S2. The raw sample B exhibited the highest leachability among all the tested samples, with HM concentrations several orders of magnitude higher measured for Cr, Mn, Co, Ni, Cu, Zn, As, Cd, and Sb. EC values were highest, ranging from 20.8 to 21.5 mS/cm in wastewater, consistent with the weight loss, as well as the chloride and sulfate concentrations measured by XRF. Additionally, it produced less alkaline leachates, with washing wastewater at a pH of 10.1. Leaching concentrations were consistent among the raw C, D and E samples. However, sample A tended to produce notably higher concentrations of Al, Cu, and Sb, along with lower concentrations of Mn, Fe, Co, Ni, Zn, and Pb.

Table 7. pH and electrical conductivity (EC) of each liquid sample, with their corresponding sample names. Note that the washing wastewater corresponds to a L/S of 40, while the TCLP leachates have an L/S of 10.

		Aqueous carbonation									
		AA	AC	BA	BC	CA	CC	DA	DC	EA	EC
pH	-	7.72	8.02	7.37	8.12	7.39	8.52	7.5	7.94	7.24	7.85
EC	mS/cm	2.77	0.696	21.5	3.75	13.67	2.03	13.76	2.61	12.65	7.86
		Water washing									
		AB	AW	BB	BW	CB	CW	DB	DW	EB	EW
pH	-	11.44	11.45	10.1	10.1	12.06	12.1	11.96	12.01	12.12	11.45
EC	mS/cm	2.5	1.634	20.8	3.76	18.08	8.82	17.12	10.04	15.84	1.634

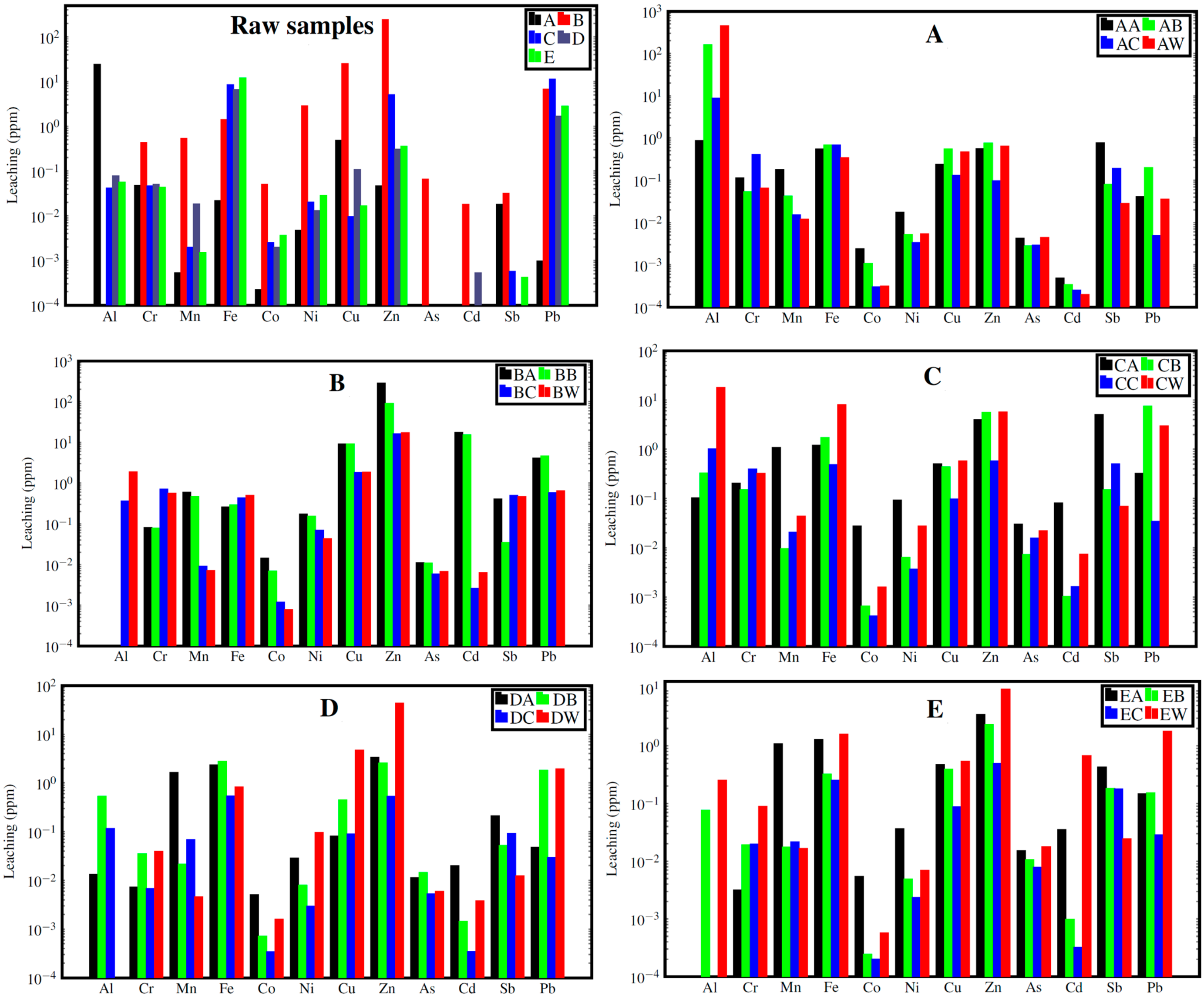

Figure 12. HM concentrations from TCLP on raw samples, carbonated samples, and wastewater from aqueous carbonation and water-washing experiments for (**A**) sample A (**B**) sample B (**C**) sample C (**D**) sample D (**E**) sample E. Note the logarithmic scale. Note that the washing wastewater correspond to an L/S of 40, while the TCLP leachates have an L/S of 10.

Table 8 presents the ratio of HM leaching concentrations between aqueous carbonation and water-washing experiments, expressed as a percentage. Overall, the results indicate that carbonation generally increases the leaching of HMs into the washing water and leads to a significant reduction in leaching during the TCLP tests. Sample A exhibited contrasting behaviour in comparison with samples C, D and E, where TCLP leachate concentrations significantly decreased after carbonation compared to water washing. On the other hand, sample B displayed comparable HM concentration values between carbonation and water washing, thus highlighting its unreactivity and similar phase compositions.

Table 8. Ratio of heavy metal leaching concentrations in both wastewater and TCLP leachates between aqueous carbonation and water-washing experiments, expressed as a percentage. An increase in leaching due to carbonation compared to water washing is indicated by a red backcolor and '+', while a reduction is indicated by a green backcolor and '−'.

		Wastewaters					**Leachates from TCLP**				
Sample Names		**A**	**B**	**C**	**D**	**E**	**A**	**B**	**C**	**D**	**E**
Experiments		**AA/AB**	**AC/AW**	**BA/BB**	**BC/BW**	**CA/CB**	**CC/CW**	**DA/DB**	**DC/DW**	**EA/EB**	**EC/EW**
Al	%	−99.5	n.d.	−69.1	−97.5	−100.0	−98.1	−80.9	−94.3	n.d.	−100.0
Cr	%	+53.6	+3.4	+26.5	−79.4	−83.6	+83.7	+21.1	+18.7	−82.6	−77.9
Mn	%	+76.5	+22.4	+99.1	+98.7	+98.4	+21.6	+20.4	−52.7	+93.3	+22.6
Fe	%	−19.7	−12.0	−29.7	−15.4	+74.8	+49.9	−11.7	−94.0	−35.2	−84.2
Co	%	+55.4	+52.2	+97.6	+86.0	+95.5	−4.5	+33.2	−74.2	−78.6	−64.5
Ni	%	+70.6	+12.6	+93.2	+72.0	+86.7	−37.8	+37.3	−86.5	−96.9	−66.3
Cu	%	−55.9	+1.3	+13.6	−82.0	+17.4	−72.3	−2.4	−83.1	−98.1	−83.7
Zn	%	−26.3	+68.3	−29.2	+24.1	+33.4	−84.7	−6.4	−90.0	−98.8	−94.9
As	%	+34.8	+1.9	+76.0	−20.6	+29.5	−33.2	−12.9	−29.6	−11.0	−55.6
Cd	%	+30.0	+13.2	+98.7	+92.8	+97.2	+21.7	−59.2	−78.2	−90.9	−100.0
Sb	%	+89.7	+91.6	+97.1	+75.2	+57.9	+85.0	+6.1	+86.4	+86.3	+86.3
Pb	%	−79.6	−11.3	−95.7	−97.4	−4.2	−86.4	−9.4	−98.8	−98.5	−98.4

However, Al and Pb were strongly stabilized in both wastewater and TCLP leachates, while Mn and Sb were mobilized, with Sb showing the most critical behaviour under carbonation. Co, Ni and Cd were highly mobilized in the wastewater but were significantly stabilized in the TCLP leachates. Conversely, Cu and Zn showed no consistent trends in the wastewater but exhibited enhanced stabilization in the TCLP leachates. As displayed slight mobilization in the wastewater, which resulted in a modest reduction in TCLP concentrations. Fe and Cr exhibited the most contrasting leaching behaviours.

After carbonation, Al predominantly exists as Al(OH)$_3$ [91,92], either as a gibbsite or amorphous form, owing to the low solubility of Al-hydroxides at pH levels of 7–8 [93]. Khan [94] reported the incorporation of As oxyanions into calcite crystals after carbonation treatment. Cd can be stabilized through octavite precipitation (CdCO$_3$) or by coprecipitation with calcite, forming (Cd,Ca)CO$_3$ [95]. Mn leaching was found to be highly pH-dependent, significantly increasing as carbonation lowered the pH [96]. Pb is the most stabilized HM during aqueous carbonation, as cerussite (PbCO$_3$) serves as a solubility-controlling mineral in the pH range 6–12 [97–101]. Notably, Pb is significantly more stabilized in APCr by wet carbonation compared to gas–solid carbonation [102]. Sb is the most critically mobilized HM, primarily attributed to romeite (CaSb$_2$O$_6$) dissolution [103,104]. Sb solubility primarily depends on pH and Ca^{2+} availability [105]. Sb may pose a potential toxic risk in secondary building materials containing MSWI residues, necessitating long-term monitoring of its release [106]. Overall, our results are consistent with previous studies. Specifically, using APCr, Baciocchi [107] reported that the main effects of carbonation on trace metal leaching included a significant decrease in the mobility of Pb, Zn, and Cu at high pH, a slight change or mobilization for Cr and Sb, and no major effects on the release of As and soluble salts.

3.2.5. Mechanism of Chromium Leaching in BA Carbonation: A Novel Perspective

Stabilizing the finer BA fractions should be further enhanced to support systematic reuse and ensure the long-term safety of BA-amended constructions. Cr and Sb are among the most critical elements in BA for HM leaching, often exceeding inert waste quality standards [108]. Other HMs may include Ba, Cu, Ni, Mo, Pb, and Zn [109–111].

Cr exists primarily in two oxidation states: Cr(III)) and Cr(VI). While Cr(VI) is widely recognized for its acute toxicity and carcinogenic potential, Cr(III) is less harmful, although it also poses health risks under certain conditions [112,113]. Using µ-XANES, De Matteis [114] detected Cr(III) only, in the finer BA grain sizes, occurring as chromite. Notably, Cr leaching behaviour during and following carbonation was more critical in comparison with other samples. Using BA, Um [115] found that Cr leaching initially increases due to the decomposition of layered double hydroxides (LDHs), ettringite and Hcl, but may decrease as Cr ions are adsorbed onto the resulting amorphous Al-material. To verify the Cr leaching control mechanism, Figures 13 and 14 show backscattered electron SEM images of Hcl and Cr-Mn-Fe oxide, respectively, in a polished section of the raw sample A.

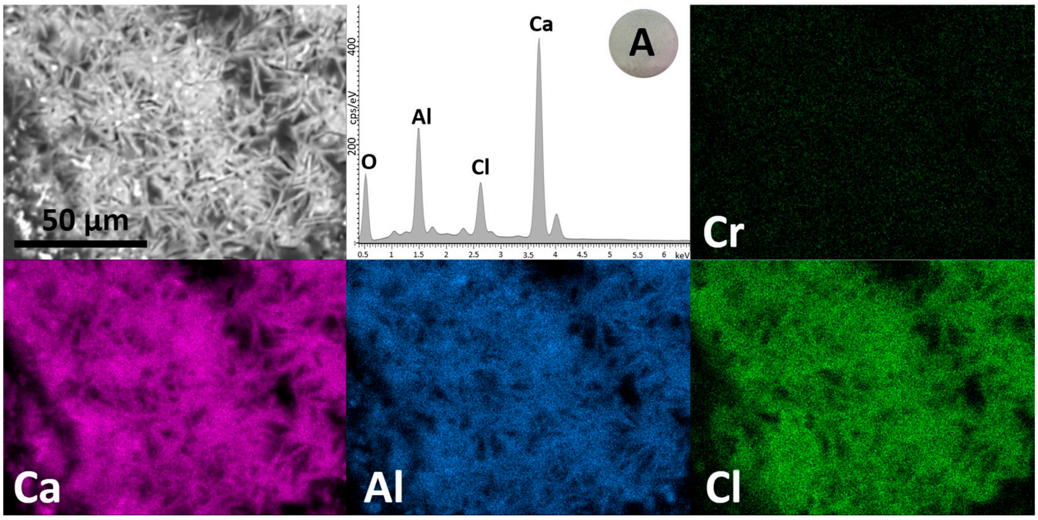

Figure 13. Backscattered electron SEM images of hydrocalumite in a raw sample A polished section. Colours identify elements, recognised by SEM-EDX mapping: magenta, Ca; blue, Al; green, Cl.

Figure 13 illustrates that no Cr was detected in the Hcl particles analyzed via EDS. Instead, Cr was concentrated in the Cr-Mn-Fe oxide particles, which were coated by Ca-aluminates (Figure 14). We attribute this coating to the dissolution-precipitation of CaO and Al_2O_3 during quenching, promoting the formation of Ca-aluminate precipitates on the surfaces of HM oxide particles (Figure 14). The presence of Cr-Mn-Fe oxide particles aligns with the known affinity of Cr for Mn-Fe oxides [116–119]. These findings indicate that in sample A, the increased leaching of Cr, Mn, and Fe during carbonation is primarily controlled by the decomposition of these Cr-Mn-Fe oxide particles, a process that is itself driven by the breakdown of the Ca-aluminate coatings. This highlights the complex interplay between mineral phases and the leaching behaviours of HMs in the carbonation process. This newly proposed mechanism is illustrated in Figure 15.

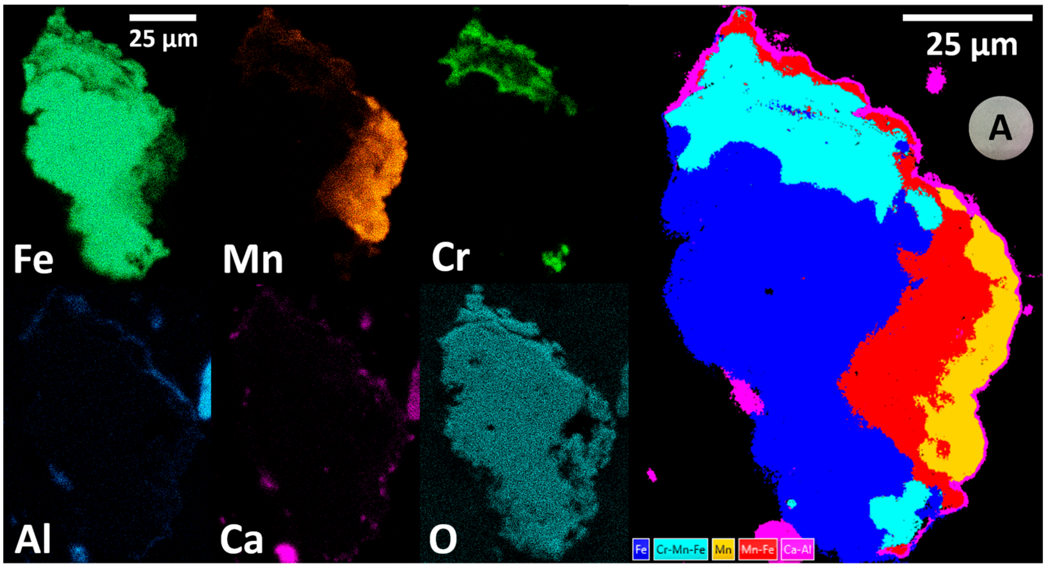

Figure 14. Backscattered electron SEM images of a Cr-Mn-Fe oxide with Ca-aluminate coating in a raw sample A polished section. Right image: Colors identify phases, recognized by SEM-EDS mapping: blue, Fe oxide; cyan, Cr-Mn-Fe oxide; yellow, Mn oxide; red, Mn-Fe oxide; magenta, Ca-aluminate.

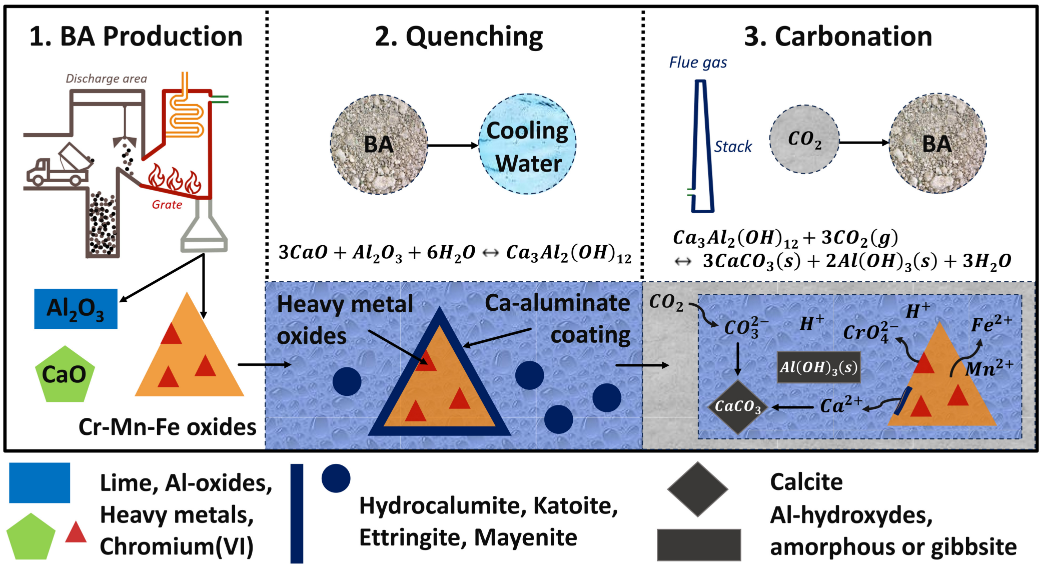

Figure 15. Proposed mechanism of chromium leaching during BA carbonation due to Ca-aluminate coating breakdown and Cr-Mn-Fe oxides decomposition. Both trivalent (Cr^{3+}) and hexavalent (CrO_4^{2-}) chromium were represented.

These findings suggest that to sustainably enhance the stabilization of fine BA fractions, metal separation techniques should be implemented prior to carbonation. Additionally, Allegrini [120] found a considerable non-recovered resource potential in fine fraction (<2 mm), where approximately 12% of the total non-ferrous potential in the BA was left. Using a similar BA fine fraction (<2 mm), Pienkoß [121] and Sierra [122] demonstrated that HMs can be recovered by enriching the denser fraction via wet density separation, yielding a metal concentrate containing Fe, Zn, Cu, Pb, Zr, Cr, Ni, Sn, W, and V. The most critical process parameters were the stroke frequency and tilt angle of the wet shaking table. Further improvement in HM enrichment could be leveraged by using dry-discharged or non-aged wet-discharged BA. Thus, particles like those shown in Figure 14 appear to be suitable candidates for density or magnetic separation, effectively reducing the leaching of Cr, Mn, and Fe. Bruno [123] showed that the EMR of Cu and Fe from BA would result in significant energy savings, reductions in CO_2 emissions, and economic profitability driven by recycling and avoided landfill costs. Indeed, Cu is known to undergo fractionation both in finer (<0.45 mm) and coarse (>4 mm) BA fractions [124]. Beikmohammadi [125] showed that average concentrations of HMs in BA, including Zn, Cu, Ba, Pb, Cr, Ni, Sn, V, As, and Sb, were higher in the <4 mm fraction, while Au and Ag were significantly higher in the <0.5 mm fraction, making their extraction economically viable. Notably, in sample A, the weight concentrations of CuO (0.25%), ZnO (0.85%), and Ag_2O (0.16%) are comparable to typical ore grades. Specifically, the average ore grade for Zn was 1.2% in 2017 [126], Cu is nearing 0.5% in 2024, although with a continued declining trend [127,128], and Ag ore grades generally fall within the range of 0.05–0.35% [129]. This positions the concentrations in sample A within the typical range of these metals in natural ores, emphasizing the growing potential of urban mining from MSW and their incineration residues.

This underscores the importance of appropriate EMR-based pre-treatment before utilizing these materials in ACT, as well as in construction or landfilling [130]. However, while carbonation results in density and strength improvement of fine BA [92], Weiksnar [131] demonstrated that EMR has minimal to no impact on the compressive strength of BA-amended concrete.

4. Conclusions

This study aims to assess the reactivity of Municipal Solid Waste Incineration (MSWI) residues in aqueous carbonation under typical production conditions. Mixtures of boiler, electrofilter, and bag filter residues were selected to compare their reactivity in terms of CO_2 absorption rates, CO_2 uptake, and resulting heavy metal (HM) leaching behaviour. The effectiveness of aqueous carbonation was compared with conventional water washing for HMs removal and stabilization, further highlighting the stabilization and mobilization effects induced by carbonation.

Results show that bag filter residues from plant 1 using lime as a sorbent are the most reactive type of MSWI residues, achieving a carbonation degree of 244.5 gCO_2/kg (sample E). In comparison, a carbonation degree of 101 gCO_2/kg was achieved for the BA fine fraction (sample A), 93 gCO_2/kg for the boiler/electrofilter APCr (sample C), 0 gCO_2/kg for the electrofilter/bag filter FA from plant 2 using sodium bicarbonate, and 167 gCO_2/kg for the mixed boiler/electrofilter/bag filter APCr from plant 3 using lime (sample D). Thus, samples from plants using lime are prime candidates for Accelerated Carbonation Technology (ACT), while MSWI residues from plants using sodium bicarbonate are unsuitable and better suited for the FLUWA/FLUREC processes focused solely on EMR.

All MSWI residues with high calcium (chloro)(hydr)oxide content exhibited similar kinetic behaviour during carbonation, as shown by the comparable trends and intensities in their CO_2 absorption rate patterns. However, contrary to common findings in the literature, BA carbonation was primarily driven by Ca-aluminates—specifically by hydrocalumite and katoite—rather than by lime. The carbonation kinetics of BA were slower due to the slower dissolution rate of Ca-aluminates compared to lime, as reflected in the BA sample's CO_2 absorption rate pattern. Despite this, the dissolution of Ca-aluminates led to a carbonation degree (101 gCO_2/kg) about three times higher than that commonly reported for BA in the literature, which normally ranges from 25 to 45 gCO_2/kg.

Overall, our results demonstrate that HM leaching significantly increases during carbonation compared to regular washing but subsequent TCLP tests indicate a relevant decrease in toxicity. The samples C, D and E showed the most substantial improvements, with marked reductions in leaching of Cr, Fe, Co, Ni, Cu, Zn, Cd, and Pb post-carbonation. However, Sb exhibits a critical leaching increase in all samples, both in wastewater and TCLP leachates. Additionally, the leaching behaviour of Fe, and especially Cr, poses significant concerns about BA carbonation. We attribute the elevated Cr, Mn, and Fe leaching during BA carbonation primarily to the decomposition of Cr-Mn-Fe oxide particles, a process driven by pH lowering and breaking down Ca-aluminate coatings on slag particles. To our knowledge, this mechanism is being reported for the first time in this work.

In conclusion, BA and APCr from plants using lime as a sorbent are successful candidates for ACT. However, additional treatments must be integrated into their waste management sequences, in order to develop a fully sustainable process, in both environmental and economical terms. Notably, integrating EMR from the fine fraction of BA through density or magnetic separation prior to carbonation has the potential to sustainably address excessive HM leaching, particularly of Fe and Cr and even potentially Sb, while recycling raw materials.

Supplementary Materials: The following supporting information can be downloaded at: https://www.mdpi.com/article/10.3390/min14121269/s1, Equations (S1)–(S6): data treatment methods with detailed formulas; Table S1: physicochemical properties and corresponding leaching limit values for the use of recycled waste; Figure S1: images of the bag filter residues (APCr), boiler + electrofilter ashes (FA), and the particle size fraction of BA; Figure S2: grain size distribution curve of bottom ash; Figure S3: XRPD and SEM-EDS patterns of sample A's magnetic fraction; Table S2: detailed HM concentrations from the TCLP analysis of raw samples, carbonated samples, and wastewater from the aqueous carbonation and water-washing experiments, Figure S4: morphology of portlandite particles used as a standard for the quantification of the carbonation degree of MSWI residues.

Author Contributions: Conceptualization, Q.W. and D.B.; methodology, Q.W. and D.B.; software, Q.W. and D.B.; validation, E.D., C.C., N.C., E.B., A.P. and L.P.; formal analysis, Q.W. and D.B.; investigation, Q.W., D.B. and S.D.F.; resources, E.D., A.P. and L.P.; data curation, Q.W.; writing—original draft preparation, Q.W.; writing—review and editing, Q.W., D.B., C.C., N.C., S.D.F., A.P. and L.P.; visualization, Q.W.; supervision, E.D., E.B., A.P. and L.P.; project administration, A.P. and L.P.; funding acquisition, A.P. and L.P. All authors have read and agreed to the published version of the manuscript.

Funding: This research was funded by the Italian Ministry for Education, University and Research (MIUR; project PRIN2017-2017L83S77) and by the Ministry for Ecological Transition (MiTE; project CLEAN), for possible applications to fly ash treatment. The APC was funded by Enrico Destefanis, Caterina Caviglia and Linda Pastero.

Data Availability Statement: The data presented in this study are available on request from the corresponding author.

Conflicts of Interest: The authors declare no conflicts of interest.

References

1. Bodor, M.; Santos, R.M.; Van Gerven, T.; Vlad, M. Recent developments and perspectives on the treatment of industrial wastes by mineral carbonation—A review. *Cent. Eur. J. Eng.* **2013**, *3*, 566–584. [CrossRef]
2. Hills, C.D.; Tripathi, N.; Carey, P.J. Mineralization technology for carbon capture, utilization, and storage. *Front. Energy Res.* **2020**, *8*, 142. [CrossRef]
3. Baciocchi, R.; Costa, G. CO_2 utilization and long-term storage in useful mineral products by carbonation of alkaline feedstocks. *Front. Energy Res.* **2021**, *9*, 592600. [CrossRef]
4. Jin, F.; Zhao, M.; Xu, M.; Mo, L. Maximising the benefits of calcium carbonate in sustainable cements: Opportunities and challenges associated with alkaline waste carbonation. *npj Mater. Sustain.* **2024**, *2*, 1. [CrossRef]
5. Gunning, P.J.; Hills, C.D.; Carey, P.J. Accelerated carbonation treatment of industrial wastes. *Waste Manag.* **2010**, *30*, 1081–1090. [CrossRef]
6. Di Maria, A.; Snellings, R.; Alaerts, L.; Quaghebeur, M.; Van Acker, K. Environmental assessment of CO2 mineralisation for sustainable construction materials. *Int. J. Greenhouse Gas Control* **2020**, *93*, 102882. [CrossRef]
7. Tiefenthaler, J.; Braune, L.; Bauer, C.; Sacchi, R.; Mazzotti, M. Technological demonstration and life cycle assessment of a negative emission value chain in the Swiss concrete sector. *Front. Clim.* **2021**, *3*, 729259. [CrossRef]
8. Zhang, N.; Chai, Y.E.; Santos, R.M.; Šiller, L. Advances in process development of aqueous CO_2 mineralisation towards scalability. *J. Environ. Chem. Eng.* **2020**, *8*, 104453. [CrossRef]
9. Wei, Y.; Shimaoka, T.; Saffarzadeh, A.; Takahashi, F. Mineralogical characterization of municipal solid waste incineration bottom ash with an emphasis on heavy metal-bearing phases. *J. Hazard. Mater.* **2011**, *187*, 534–543. [CrossRef]
10. Nam, S.Y. Accelerated carbonation of municipal solid waste incineration bottom ash for CO_2 sequestration. *Geosyst. Eng.* **2012**, *15*, 305–311. [CrossRef]
11. Baciocchi, R.; Costa, G.; Di Bartolomeo, E.; Polettini, A.; Pomi, R. The effects of accelerated carbonation on CO_2 uptake and metal release from incineration APC residues. *Waste Manag.* **2009**, *29*, 2994–3003. [CrossRef] [PubMed]

12. Rocca, S.; van Zomeren, A.; Costa, G.; Dijkstra, J.J.; Comans, R.N.; Lombardi, F. Characterisation of major component leaching and buffering capacity of RDF incineration and gasification bottom ash in relation to reuse or disposal scenarios. *Waste Manag.* **2012**, *32*, 759–768. [CrossRef] [PubMed]
13. Di Gianfilippo, M.; Costa, G.; Pantini, S.; Allegrini, E.; Lombardi, F.; Astrup, T.F. LCA of management strategies for RDF incineration and gasification bottom ash based on experimental leaching data. *Waste Manag.* **2016**, *47*, 285–298. [CrossRef]
14. Jagodzińska, K.; Mroczek, K.; Nowińska, K.; Gołombek, K.; Kalisz, S. The impact of additives on the retention of heavy metals in the bottom ash during RDF incineration. *Energy* **2019**, *183*, 854–868. [CrossRef]
15. Mlonka-Mędrala, A.; Dziok, T.; Magdziarz, A.; Nowak, W. Composition and properties of fly ash collected from a multifuel fluidized bed boiler co-firing refuse derived fuel (RDF) and hard coal. *Energy* **2021**, *234*, 121229. [CrossRef]
16. Shehata, N.; Obaideen, K.; Sayed, E.T.; Abdelkareem, M.A.; Mahmoud, M.S.; El-Salamony, A.H.R.; Mahmoud, M.H.; Olabi, A.G. Role of refuse-derived fuel in circular economy and sustainable development goals. *Process Saf. Environ. Prot.* **2022**, *163*, 558–573. [CrossRef]
17. Wen, H.; Gao, J.; Wang, X.; He, Y.; Li, J.; Gu, L.; Zhao, Z.; Haixiang, Y.; Xu, S. Mechanistic insights into temperature-driven retention and speciation changes of heavy metals (HMs) in ash residues from Co-combustion of refuse-derived fuel (RDF) and red mud. *J. Environ. Manag.* **2024**, *368*, 121967. [CrossRef] [PubMed]
18. Nikravan, M.; Ramezanianpour, A.A.; Maknoon, R. Study on physiochemical properties and leaching behavior of residual ash fractions from a municipal solid waste incinerator (MSWI) plant. *J. Environ. Manag.* **2020**, *260*, 110042. [CrossRef] [PubMed]
19. Bernasconi, D.; Caviglia, C.; Destefanis, E.; Agostino, A.; Boero, R.; Marinoni, N.; Pavese, A. Influence of speciation distribution and particle size on heavy metal leaching from MSWI fly ash. *Waste Manag.* **2022**, *138*, 318–327. [CrossRef]
20. Jiang, J.; Tian, S.; Zhang, C. Influence of SO_2 in incineration flue gas on the sequestration of CO_2 by municipal solid waste incinerator fly ash. *J. Environ. Sci.* **2013**, *25*, 735–740. [CrossRef]
21. Viet, D.B.; Chan, W.P.; Phua, Z.H.; Ebrahimi, A.; Abbas, A.; Lisak, G. The use of fly ashes from waste-to-energy processes as mineral CO_2 sequesters and supplementary cementitious materials. *J. Hazard. Mater.* **2020**, *398*, 122906. [CrossRef] [PubMed]
22. Bandarra, B.S.; Silva, S.; Pereira, J.L.; Martins, R.C.; Quina, M.J. A Study on the Classification of a Mirror Entry in the European List of Waste: Incineration Bottom Ash from Municipal Solid Waste. *Sustainability* **2022**, *14*, 10352. [CrossRef]
23. De Matteis, C.; Mantovani, L.; Tribaudino, M.; Bernasconi, A.; Destefanis, E.; Caviglia, C.; Funari, V. Sequential extraction procedure of municipal solid waste incineration (MSWI) bottom ash targeting grain size and the amorphous fraction. *Front. Environ. Sci.* **2023**, *11*, 1254205. [CrossRef]
24. Yeo, R.J.; Sng, A.; Wang, C.; Tao, L.; Zhu, Q.; Bu, J. Strategies for heavy metals immobilization in municipal solid waste incineration bottom ash: A critical review. *Rev. Environ. Sci. Bio/Technol.* **2024**, *23*, 503–568. [CrossRef]
25. Chandler, A.J.; Eighmy, T.T.; Hjelmar, O.; Kosson, D.S.; Sawell, S.E.; Vehlow, J.; Hartlén, J. *Municipal Solid Waste Incinerator Residues*; Elsevier: Amsterdam, The Netherlands, 1997. Available online: https://www.elsevier.com/books/municipalsolid-waste-incinerator-residues/chandler/978-0-444-82563-6 (accessed on 24 June 2024).
26. De Boom, A.; Degrez, M. Belgian MSWI fly ashes and APC residues: A characterisation study. *Waste Manag.* **2012**, *32*, 1163–1170. [CrossRef]
27. Raclavska, H.; Matysek, D.; Raclavsky, K.; Juchelkova, D. Geochemistry of fly ash from desulphurisation process performed by sodium bicarbonate. *Fuel Process. Technol.* **2010**, *91*, 150–157. [CrossRef]
28. Lu, S.; Ji, Y.; Buekens, A.; Ma, Z.; Jin, Y.; Li, X.; Yan, J. Activated carbon treatment of municipal solid waste incineration flue gas. *Waste Manag. Res.* **2013**, *31*, 169–177. [CrossRef]
29. Ling, Y.; Gu, Q.; Jin, B. Density functional theory study on the formation mechanism of CaClOH in municipal solid waste incineration fly ash. *Environ. Sci. Pollut. Res.* **2023**, *30*, 106514–106532. [CrossRef]
30. Meima, J.A.; van der Weijden, R.D.; Eighmy, T.T.; Comans, R.N. Carbonation processes in municipal solid waste incinerator bottom ash and their effect on the leaching of copper and molybdenum. *Appl. Geochem.* **2002**, *17*, 1503–1513. [CrossRef]
31. Baciocchi, R.; Costa, G.; Lategano, E.; Marini, C.; Polettini, A.; Pomi, R.; Rocca, S. Accelerated carbonation of different size fractions of bottom ash from RDF incineration. *Waste Manag.* **2010**, *30*, 1310–1317. [CrossRef]
32. Brück, F.; Schnabel, K.; Mansfeldt, T.; Weigand, H. Accelerated carbonation of waste incinerator bottom ash in a rotating drum batch reactor. *J. Environ. Chem. Eng.* **2018**, *6*, 5259–5268. [CrossRef]
33. Campo, F.P.; Tua, C.; Biganzoli, L.; Pantini, S.; Grosso, M. Natural and enhanced carbonation of lime in its different applications: A review. *Environ. Technol. Rev.* **2021**, *10*, 224–237. [CrossRef]
34. Jozewicz, W.; Gullett, B.K. Reaction mechanisms of dry Ca-based sorbents with gaseous HCl. *Ind. Eng. Chem. Res.* **1995**, *34*, 607–612. [CrossRef]
35. Chyang, C.S.; Han, Y.L.; Zhong, Z.C. Study of HCl absorption by CaO at high temperature. *Energy Fuels* **2009**, *23*, 3948–3953. [CrossRef]
36. Jaschik, J.; Jaschik, M.; Warmuziński, K. The utilisation of fly ash in CO_2 mineral carbonation. *Chem. Process Eng.* **2016**, *37*, 29–39. [CrossRef]
37. Gu, Q.; Wang, T.; Wu, W.; Wang, D.; Jin, B. Influence of pretreatments on accelerated dry carbonation of MSWI fly ash under medium temperatures. *Chem. Eng. J.* **2021**, *414*, 128756. [CrossRef]

38. Chen, J.; Fu, C.; Mao, T.; Shen, Y.; Li, M.; Lin, X.; Yan, J. Study on the accelerated carbonation of MSWI fly ash under ultrasonic excitation: CO_2 capture, heavy metals solidification, mechanism and geochemical modelling. *Chem. Eng. J.* **2022**, *450*, 138418. [CrossRef]
39. Sorrentino, G.P.; Guimarães, R.; Valentim, B.; Bontempi, E. The Influence of Liquid/Solid Ratio and Pressure on the Natural and Accelerated Carbonation of Alkaline Wastes. *Minerals* **2023**, *13*, 1080. [CrossRef]
40. Brück, F.; Mansfeldt, T.; Weigand, H. Flow-through carbonation of waste incinerator bottom ash in a rotating drum batch reactor: Role of specific CO_2 supply, mixing tools and fill level. *J. Environ. Chem. Eng.* **2019**, *7*, 102975. [CrossRef]
41. Brück, F.; Ufer, K.; Mansfeldt, T.; Weigand, H. Continuous-feed carbonation of waste incinerator bottom ash in a rotating drum reactor. *Waste Manag.* **2019**, *99*, 135–145. [CrossRef]
42. Schnabel, K.; Brück, F.; Mansfeldt, T.; Weigand, H. Full-scale accelerated carbonation of waste incinerator bottom ash under continuous-feed conditions. *Waste Manag.* **2021**, *125*, 40–48. [CrossRef] [PubMed]
43. Lim, M.; Han, G.C.; Ahn, J.W.; You, K.S. Environmental remediation and conversion of carbon dioxide (CO_2) into useful green products by accelerated carbonation technology. *Int. J. Environ. Res. Public Health* **2010**, *7*, 203–228. [CrossRef] [PubMed]
44. Lee, H.W.; Han, C.; Whan, A.J. CO_2 sequestration of real flue gases from landfill municipal solid waste incineration (MSWI) -Pilot scale demonstration. *Int. J. Phys. Appl. Sci.* **2015**, *2*, 54–63.
45. Um, N.; Ahn, J.W. Effects of two different accelerated carbonation processes on MSWI bottom ash. *Process Saf. Environ. Prot.* **2017**, *111*, 560–568. [CrossRef]
46. Gunning, P.J.; Hills, C.D.; Carey, P.J. Production of lightweight aggregate from industrial waste and carbon dioxide. *Waste Manag.* **2009**, *29*, 2722–2728. [CrossRef] [PubMed]
47. Quina, M.J.; Garcia, R.; Simões, A.S.; Quinta-Ferreira, R.M. Life cycle assessment of lightweight aggregates produced with ashes from municipal solid waste incineration. *J. Mater. Cycles Waste Manag.* **2020**, *22*, 1922–1931. [CrossRef]
48. Bernasconi, D.; Viani, A.; Zárybnická, L.; Mácová, P.; Bordignon, S.; Caviglia, C.; Pavese, A. Phosphate-based geopolymer: Influence of municipal solid waste fly ash introduction on structure and compressive strength. *Ceram. Int.* **2023**, *49*, 22149–22159. [CrossRef]
49. Bernasconi, D.; Viani, A.; Zárybnická, L.; Mácová, P.; Bordignon, S.; Das, G.; Pavese, A. Reactivity of MSWI-fly ash in Mg-K-phosphate cement. *Constr. Build. Mater.* **2023**, *409*, 134082. [CrossRef]
50. Shen, X.; He, H.; He, C.; Li, B.; Luo, W.; Ren, P. Low-carbon blended cement containing wet carbonated municipal solid waste incineration fly ash and mechanically activated coal fly ash. *Case Stud. Constr. Mater.* **2024**, *21*, e03671. [CrossRef]
51. Lu, M.; Ge, W.; Xia, Y.; Sun, C.; Lin, X.; Tsang, D.C.; Yan, J. Upcycling MSWI fly ash into green binders via flue gas-enhanced wet carbonation. *J. Clean. Prod.* **2024**, *440*, 141013. [CrossRef]
52. Quina, M.J.; Bontempi, E.; Bogush, A.; Schlumberger, S.; Weibel, G.; Braga, R.; Lederer, J. Technologies for the management of MSW incineration ashes from gas cleaning: New perspectives on recovery of secondary raw materials and circular economy. *Sci. Total Environ.* **2018**, *635*, 526–542. [CrossRef]
53. Langer, M. Use of solution-mined caverns in salt for oil and gas storage and toxic waste disposal in Germany. *Eng. Geol.* **1993**, *35*, 183–190. [CrossRef]
54. Zhang, S.; Zhao, T.; Li, Y.; Li, Z.; Li, H.; Zhang, B.; Ni, W. The effects and solidification characteristics of municipal solid waste incineration fly ash-slag-tailing based backfill blocks in underground mine condition. *Constr. Build. Mater.* **2024**, *420*, 135508. [CrossRef]
55. Kashefi, K.; Pardakhti, A.; Shafiepour, M.; Hemmati, A. Process optimization for integrated mineralization of carbon dioxide and metal recovery of red mud. *J. Environ. Chem. Eng.* **2020**, *8*, 103638. [CrossRef]
56. Hong, S.; Moon, S.; Sim, G.; Park, Y. Metal recovery from iron slag via pH swing-assisted carbon mineralization with various organic ligands. *J. CO2 Util.* **2023**, *69*, 102418. [CrossRef]
57. Wang, F.; Dreisinger, D. An integrated process of CO_2 mineralization and selective nickel and cobalt recovery from olivine and laterites. *Chem. Eng. J.* **2023**, *451*, 139002. [CrossRef]
58. Wang, F.; Dreisinger, D. Enhanced CO_2 mineralization and selective critical metal extraction from olivine and laterites. *Sep. Purif. Technol.* **2023**, *321*, 124268. [CrossRef]
59. Wang, F.; Dreisinger, D.; Xiao, Y. Accelerated CO_2 mineralization and utilization for selective battery metals recovery from olivine and laterites. *J. Clean. Prod.* **2023**, *393*, 136345. [CrossRef]
60. Kumar, R.; Chung, W.J.; Khan, M.A.; Son, M.; Park, Y.K.; Lee, S.S.; Jeon, B.H. Breakthrough innovations in carbon dioxide mineralization for a sustainable future. *Rev. Environ. Sci. Bio/Technol.* **2024**, *23*, 739–799. [CrossRef]
61. Caviglia, C.; Destefanis, E.; Pastero, L.; Bernasconi, D.; Bonadiman, C.; Pavese, A. MSWI fly ash multiple washing: Kinetics of dissolution in water, as function of time, temperature and dilution. *Minerals* **2022**, *12*, 742. [CrossRef]
62. Brück, F.; Fröhlich, C.; Mansfeldt, T.; Weigand, H. A fast and simple method to monitor carbonation of MSWI bottom ash under static and dynamic conditions. *Waste Manag.* **2018**, *78*, 588–594. [CrossRef] [PubMed]
63. Wehrung, Q.; Pastero, L.; Bernasconi, D.; Cotellucci, A.; Bruno, M.; Cavagna, S.; Pavese, A. Impact of Operational Parameters on the CO_2 Absorption Rate in $Ca(OH)_2$ Aqueous Carbonation–Implications for Process Efficiency. *Energy Fuels* **2024**, *38*, 16678–16691. [CrossRef]

64. Wehrung, Q.; Bernasconi, D.; Destefanis, E.; Caviglia, C.; Curetti, N.; Bicchi, E.; Pavese, A.; Pastero, L. Carbonation washing of waste incinerator air pollution control residues under wastewater reuse conditions. *J. Environ. Chem. Eng.* **2024**. *submitted*.
65. Caviglia, C.; Confalonieri, G.; Corazzari, I.; Destefanis, E.; Mandrone, G.; Pastero, L.; Pavese, A. Effects of particle size on properties and thermal inertization of bottom ashes (MSW of Turin's incinerator). *Waste Manag.* **2019**, *84*, 340–354. [CrossRef]
66. Wolffers, M.; Eggenberger, U.; Schlumberger, S.; Churakov, S.V. Characterization of MSWI fly ashes along the flue gas cooling path and implications on heavy metal recovery through acid leaching. *Waste Manag.* **2021**, *134*, 231–240. [CrossRef]
67. Deuster, E.V.; Mensing, A.; Jiang, M.X.; Majdeski, H. Cleaning of flue gas from solid waste incinerator plants by wet/semi-dry process. *Environ. Prog.* **1994**, *13*, 149–153. [CrossRef]
68. *LS EN-12457*; Characterisation of Waste–Leaching–Compliance Test for Leaching of Granular Waste Materials and Sludges. European Committee for Standardization: Brussels, Belgium, 2002.
69. Gevers, B.R.; Labuschagné, F.J. Green synthesis of hydrocalumite (CaAl-OH-LDH) from $Ca(OH)_2$ and $Al(OH)_3$ and the parameters that influence its formation and speciation. *Crystals* **2020**, *10*, 672. [CrossRef]
70. Gácsi, A.; Kutus, B.; Kónya, Z.; Kukovecz, Á.; Pálinkó, I.; Sipos, P. Estimation of the solubility product of hydrocalumite–hydroxide, a layered double hydroxide with the formula of $[Ca_2Al(OH)_6]OH{\cdot}nH_2O$. *J. Phys. Chem. Solids* **2016**, *98*, 167–173. [CrossRef]
71. Jiménez, A.; Rives, V.; Vicente, M.A. Thermal study of the hydrocalumite–katoite–calcite system. *Thermochim. Acta* **2022**, *713*, 179242. [CrossRef]
72. Polettini, A.; Pomi, R. The leaching behavior of incinerator bottom ash as affected by accelerated ageing. *J. Hazard. Mater.* **2004**, *113*, 209–215. [CrossRef] [PubMed]
73. Dou, X.; Ren, F.; Nguyen, M.Q.; Ahamed, A.; Yin, K.; Chan, W.P.; Chang, V.W.C. Review of MSWI bottom ash utilization from perspectives of collective characterization, treatment and existing application. *Renew. Sustain. Energy Rev.* **2017**, *79*, 24–38. [CrossRef]
74. Alam, Q.; Schollbach, K.; Rijnders, M.; van Hoek, C.; van der Laan, S.; Brouwers, H.J.H. The immobilization of potentially toxic elements due to incineration and weathering of bottom ash fines. *J. Hazard. Mater.* **2019**, *379*, 120798. [CrossRef]
75. Zhao, S.; Zhang, S.; Liang, X.; Li, J.; Liu, C.; Ji, F.; Sun, Z. Transformation and environmental chemical characteristics of hazardous trace elements in an 800 t/d waste incineration thermal power plant. *Sci. Total Environ.* **2024**, *918*, 170693. [CrossRef] [PubMed]
76. Moon, D.H.; Wazne, M. Impact of brownmillerite hydration on Cr (VI) sequestration in chromite ore processing residue. *Geosci. J.* **2011**, *15*, 287–296. [CrossRef]
77. Sorrentino, G.P.; Zanoletti, A.; Ducoli, S.; Zacco, A.; Iora, P.; Invernizzi, C.M.; Bontempi, E. Accelerated and natural carbonation of a municipal solid waste incineration (MSWI) fly ash mixture: Basic strategies for higher carbon dioxide sequestration and reliable mass quantification. *Environ. Res.* **2023**, *217*, 114805. [CrossRef]
78. Goni, S.; Guerrero, A. Accelerated carbonation of Friedel's salt in calcium aluminate cement paste. *Cem. Concr. Res.* **2003**, *33*, 21–26. [CrossRef]
79. Zhang, Z.; Zheng, K.; Chen, L.; Yuan, Q. Review on accelerated carbonation of calcium-bearing minerals: Carbonation behaviors, reaction kinetics, and carbonation efficiency improvement. *J. Build. Eng.* **2024**, *86*, 108826. [CrossRef]
80. Renforth, P. The negative emission potential of alkaline materials. *Nat. Commun.* **2019**, *10*, 1401. [CrossRef] [PubMed]
81. Schnabel, K.; Brück, F.; Pohl, S.; Mansfeldt, T.; Weigand, H. Technically exploitable mineral carbonation potential of four alkaline waste materials and effects on contaminant mobility. *Greenhouse Gases Sci. Technol.* **2021**, *11*, 506–519. [CrossRef]
82. Zhang, J.; Mao, Y.; Jin, Y.; Wang, X.; Li, J.; Yang, S.; Wang, W. Highly efficient carbonation and dechlorination using flue gas micro-nano bubble for municipal solid waste incineration fly ash pretreatment and its applicability to sulfoaluminate cementitious materials. *J. Environ. Manag.* **2024**, *353*, 120163. [CrossRef] [PubMed]
83. Suzuki, T.; Kawai, T.; Kamijima, Y.; Shinohara, S.; Tanaka, M. Application of ultrafine bubbles for enhanced carbonation of municipal solid waste incineration ash during direct aqueous carbonation. *Next Sustain.* **2024**, *3*, 100020. [CrossRef]
84. Doka, G. *Life Cycle Inventories of Municipal Waste Incineration with Residual Landfill & FLUWA Filter Ash Treatment*; Doka Life Cycle Assessments: Zurich, Switzerland, 2015.
85. Van Gerven, T.; Van Keer, E.; Arickx, S.; Jaspers, M.; Wauters, G.; Vandecasteele, C. Carbonation of MSWI-bottom ash to decrease heavy metal leaching, in view of recycling. *Waste Manag.* **2005**, *25*, 291–300. [CrossRef]
86. Rendek, E.; Ducom, G.; Germain, P. Carbon dioxide sequestration in municipal solid waste incinerator (MSWI) bottom ash. *J. Hazard. Mater.* **2006**, *128*, 73–79. [CrossRef] [PubMed]
87. Mantovani, L.; Tribaudino, M.; Matteis, C.D.; Funari, V. Particle size and potential toxic element speciation in municipal solid waste incineration (MSWI) bottom ash. *Sustainability* **2021**, *13*, 1911. [CrossRef]
88. Loginova, E.; Volkov, D.S.; Van De Wouw, P.M.; Florea, M.V.; Brouwers, H.J. Detailed characterization of particle size fractions of municipal solid waste incineration bottom ash. *J. Clean. Prod.* **2019**, *207*, 866–874. [CrossRef]
89. Destefanis, E.; Caviglia, C.; Bernasconi, D.; Bicchi, E.; Boero, R.; Bonadiman, C.; Confalonieri, G.; Corazzari, I.; Mandrone, G.; Pastero, L.; et al. Valorization of MSWI bottom ash as a function of particle size distribution, using steam washing. *Sustainability* **2020**, *12*, 9461. [CrossRef]

90. Chiang, Y.W.; Ghyselbrecht, K.; Santos, R.M.; Meesschaert, B.; Martens, J.A. Synthesis of zeolitic-type adsorbent material from municipal solid waste incinerator bottom ash and its application in heavy metal adsorption. *Catal. Today* **2012**, *190*, 23–30. [CrossRef]
91. Um, N. Effect of Cl removal in MSWI bottom ash via carbonation with CO_2 and decomposition kinetics of Friedel's salt. *Mater. Trans.* **2019**, *60*, 837–844. [CrossRef]
92. Sun, X.; Xu, B.; Yi, Y. Effects of accelerated carbonation on fine incineration bottom ash: CO_2 uptake, strength improvement, densification, and heavy metal immobilization. *J. Clean. Prod.* **2024**, *475*, 143714. [CrossRef]
93. Zhang, Y.; Cetin, B.; Likos, W.J.; Edil, T.B. Impacts of pH on leaching potential of elements from MSW incineration fly ash. *Fuel* **2016**, *184*, 815–825. [CrossRef]
94. Khan, M.D.; Song, Y.; Shakya, S.; Lim, C.; Ahn, J.W. In situ carbonation mediated immobilization of arsenic oxyanions. *J. Mol. Liq.* **2023**, *383*, 121911. [CrossRef]
95. Kim, J.J.; Lee, S.S.; Fenter, P.; Myneni, S.C.; Nikitin, V.; Peters, C.A. Carbonate coprecipitation for Cd and Zn treatment and evaluation of heavy metal stability under acidic conditions. *Environ. Sci. Technol.* **2023**, *57*, 3104–3113. [CrossRef]
96. Qin, J.; Zhang, Y.; Yi, Y.; Fang, M. Carbonation of municipal solid waste gasification fly ash: Effects of pre-washing and treatment period on carbon capture and heavy metal immobilization. *Environ. Pollut.* **2022**, *308*, 119662. [CrossRef] [PubMed]
97. Costa, G.; Baciocchi, R.; Polettini, A.; Pomi, R.; Hills, C.D.; Carey, P.J. Current status and perspectives of accelerated carbonation processes on municipal waste combustion residues. *Environ. Monit. Assess.* **2007**, *135*, 55–75. [CrossRef]
98. Jianguo, J.; Maozhe, C.; Yan, Z.; Xin, X. Pb stabilization in fresh fly ash from municipal solid waste incinerator using accelerated carbonation technology. *J. Hazard. Mater.* **2009**, *161*, 1046–1051. [CrossRef]
99. Ni, P.; Xiong, Z.; Tian, C.; Li, H.; Zhao, Y.; Zhang, J.; Zheng, C. Influence of carbonation under oxy-fuel combustion flue gas on the leachability of heavy metals in MSWI fly ash. *Waste Manag.* **2017**, *67*, 171–180. [CrossRef]
100. Bogush, A.A.; Stegemann, J.A.; Roy, A. Changes in composition and lead speciation due to water washing of air pollution control residue from municipal waste incineration. *J. Hazard. Mater.* **2019**, *361*, 187–199. [CrossRef]
101. Liu, Y.; Molinari, S.; Dalconi, M.C.; Valentini, L.; Bellotto, M.P.; Ferrari, G.; Artioli, G. Mechanistic insights into Pb and sulfates retention in ordinary Portland cement and aluminous cement: Assessing the contributions from binders and solid waste. *J. Hazard. Mater.* **2023**, *458*, 131849. [CrossRef] [PubMed]
102. Baciocchi, R.; Polettini, A.; Pomi, R.; Prigiobbe, V.; Von Zedwitz, V.N.; Steinfeld, A. CO_2 sequestration by direct gas− solid carbonation of air pollution control (APC) residues. *Energy Fuels* **2006**, *20*, 1933–1940. [CrossRef]
103. Cornelis, G.; Van Gerven, T.; Vandecasteele, C. Antimony leaching from MSWI bottom ash: Modelling of the effect of pH and carbonation. *Waste Manag.* **2012**, *32*, 278–286. [CrossRef] [PubMed]
104. Cornelis, G.; Van Gerven, T.; Snellings, R.; Verbinnen, B.; Elsen, J.; Vandecasteele, C. Stability of pyrochlores in alkaline matrices: Solubility of calcium antimonate. *Appl. Geochem.* **2011**, *26*, 809–817. [CrossRef]
105. Verbinnen, B.; Van Caneghem, J.; Billen, P.; Vandecasteele, C. Long term leaching behavior of antimony from MSWI bottom ash: Influence of mineral additives and of organic acids. *Waste Biomass Valor.* **2017**, *8*, 2545–2552. [CrossRef]
106. Vogel, C.; Scholz, P.; Kalbe, U.; Caliebe, W.; Tayal, A.; Vasala, S.J.; Simon, F.G. Speciation of antimony and vanadium in municipal solid waste incineration ashes analyzed by XANES spectroscopy. *J. Mater. Cycles Waste Manag.* **2024**, *26*, 2152–2158. [CrossRef]
107. Baciocchi, R.; Costa, G.; Polettini, A.; Pomi, R.; Prigiobbe, V. Comparison of different reaction routes for carbonation of APC residues. *Energy Procedia* **2009**, *1*, 4851–4858. [CrossRef]
108. Costa, G.P. Enhanced Separation of Incinerator Bottom Ash: Composition and Environmental Behaviour of Separated Mineral and Weakly Magnetic Fractions. *Waste Biomass Valor.* **2020**, *11*, 7079–7095. [CrossRef]
109. Santos, R.M.; Mertens, G.; Salman, M.; Cizer, Ö.; Van Gerven, T. Comparative study of ageing, heat treatment and accelerated carbonation for stabilization of municipal solid waste incineration bottom ash in view of reducing regulated heavy metal/metalloid leaching. *J. Environ. Manag.* **2013**, *128*, 807–821. [CrossRef] [PubMed]
110. Yin, K.; Chan, W.P.; Dou, X.; Lisak, G.; Chang, V.W.C. Kinetics and modeling of trace metal leaching from bottom ashes dominated by diffusion or advection. *Sci. Total Environ.* **2020**, *719*, 137203. [CrossRef] [PubMed]
111. Mantovani, L.; De Matteis, C.; Tribaudino, M.; Boschetti, T.; Funari, V.; Dinelli, E.; Pelagatti, P. Grain size and mineralogical constraints on leaching in the bottom ashes from municipal solid waste incineration: A comparison of five plants in northern Italy. *Front. Environ. Sci.* **2023**, *11*, 1179272. [CrossRef]
112. Khan, F.H.; Ambreen, K.; Fatima, G.; Kumar, S. Assessment of health risks with reference to oxidative stress and DNA damage in chromium exposed population. *Sci. Total Environ.* **2012**, *430*, 68–74. [CrossRef]
113. Naz, A.; Mishra, B.K.; Gupta, S.K. Human health risk assessment of chromium in drinking water: A case study of Sukinda chromite mine, Odisha, India. *Expos. Health* **2016**, *8*, 253–264. [CrossRef]
114. De Matteis, C.; Pollastri, S.; Mantovani, L.; Tribaudino, M. Potentially toxic elements speciation in bottom ashes from a municipal solid waste incinerator: A combined SEM-EDS, μ-XRF and μ-XANES study. *Environ. Adv.* **2024**, *15*, 100453. [CrossRef]
115. Um, N.; Nam, S.Y.; Ahn, J.W. Effect of accelerated carbonation on the leaching behavior of Cr in municipal solid waste incinerator bottom ash and the carbonation kinetics. *Mater. Trans.* **2013**, *54*, 1510–1516. [CrossRef]

116. Luther, S.; Brogfeld, N.; Kim, J.; Parsons, J.G. Study of the thermodynamics of chromium (III) and chromium (VI) binding to iron (II/III) oxide or magnetite or ferrite and manganese (II) iron (III) oxide or jacobsite or manganese ferrite nanoparticles. *Colloid Interface Sci.* **2013**, *400*, 97–103. [CrossRef] [PubMed]
117. Hai, J.; Liu, L.; Tan, W.; Hao, R.; Qiu, G. Catalytic oxidation and adsorption of Cr(III) on iron-manganese nodules under oxic conditions. *J. Hazard. Mater.* **2020**, *390*, 122166. [CrossRef]
118. Yang, C.; Ju, T.; Wang, X.; Ji, Y.; Yang, C.; Lv, H.; Fan, Y. The preparation of a novel iron/manganese binary oxide for the efficient removal of hexavalent chromium [Cr (vi)] from aqueous solutions. *RSC Adv.* **2020**, *10*, 10612–10623. [CrossRef] [PubMed]
119. Ouma, L.; Pholosi, A.; Onani, M. Optimizing Cr (VI) adsorption parameters on magnetite (Fe_3O_4) and manganese doped magnetite (MnxFe(3-x)O4) nanoparticles. *Phys. Sci. Rev.* **2023**, *8*, 3885–3895. [CrossRef]
120. Allegrini, E.; Maresca, A.; Olsson, M.E.; Holtze, M.S.; Boldrin, A.; Astrup, T.F. Quantification of the resource recovery potential of municipal solid waste incineration bottom ashes. *Waste Manag.* **2014**, *34*, 1627–1636. [CrossRef]
121. Pienkoß, F.; Abis, M.; Bruno, M.; Grönholm, R.; Hoppe, M.; Kuchta, K.; Simon, F.G. Heavy metal recovery from the fine fraction of solid waste incineration bottom ash by wet density separation. *J. Mater. Cycles Waste Manag.* **2022**, *24*, 364–377. [CrossRef]
122. Sierra, H.M.; Šyc, M.; Korotenko, E. Wet shaking table operating parameters optimization for maximizing metal recovery from incineration bottom ash fine fraction. *Waste Manag.* **2024**, *174*, 539–548. [CrossRef] [PubMed]
123. Bruno, M.; Abis, M.; Kuchta, K.; Simon, F.G.; Grönholm, R.; Hoppe, M.; Fiore, S. Material flow, economic and environmental assessment of municipal solid waste incineration bottom ash recycling potential in Europe. *J. Clean. Prod.* **2021**, *317*, 128511. [CrossRef]
124. Yao, J.; Kong, Q.; Zhu, H.; Long, Y.; Shen, D. Content and fractionation of Cu, Zn and Cd in size fractionated municipal solid waste incineration bottom ash. *Ecotoxicol. Environ. Saf.* **2013**, *94*, 131–137. [CrossRef] [PubMed]
125. Beikmohammadi, M.; Yaghmaeian, K.; Nabizadeh, R.; Mahvi, A.H. Analysis of heavy metal, rare, precious, and metallic element content in bottom ash from municipal solid waste incineration in Tehran based on particle size. *Sci. Rep.* **2023**, *13*, 16044. [CrossRef]
126. Mudd, G.M.; Jowitt, S.M.; Werner, T.T. The world's lead-zinc mineral resources: Scarcity, data, issues and opportunities. *Ore Geol. Rev.* **2017**, *80*, 1160–1190. [CrossRef]
127. Northey, S.; Mohr, S.; Mudd, G.M.; Weng, Z.; Giurco, D. Modelling future copper ore grade decline based on a detailed assessment of copper resources and mining. *Resour. Conserv. Recycl.* **2014**, *83*, 190–201. [CrossRef]
128. Liu, L.; Zhang, L.; Jiang, S.; Yuan, Z.; Chen, J. Global copper cycles in the anthroposphere since the 1960s. *Resour. Conserv. Recycl.* **2023**, *199*, 107294. [CrossRef]
129. Zhang, H.; Yu, H.; Sun, W.; Lin, S.; Zhang, C. Beneficiation of silver and silver-bearing lead–zinc ores: A review. *Miner. Eng.* **2024**, *208*, 108608. [CrossRef]
130. Xia, Y.; He, P.; Shao, L.; Zhang, H. Metal distribution characteristic of MSWI bottom ash in view of metal recovery. *J. Environ. Sci.* **2017**, *52*, 178–189. [CrossRef] [PubMed]
131. Weiksnar, K.D.; Marks, E.J.; Deaderick, M.J.; Meija-Ruiz, I.; Ferraro, C.C.; Townsend, T.G. Impacts of advanced metals recovery on municipal solid waste incineration bottom ash: Aggregate characteristics and performance in Portland limestone cement concrete. *Waste Manag.* **2024**, *187*, 70–78. [CrossRef] [PubMed]